THESIS

INSTRUMENTATION FOR ULTRA-INTENSE LASER MATTER INTERACTION STUDIES AT HIGH REPETITION RATES

Submitted by

Ryan Nedbailo

Department of Electrical and Computer Engineering

In partial fulfillment of the requirements

For the Degree of Master of Science

Colorado State University

Fort Collins, Colorado

Fall 2022

Master's Committee:

Advisor: Jorge Rocca

Mario Marconi
Azer Yalin

ABSTRACT

INSTRUMENTATION FOR ULTRA-INTENSE LASER MATTER INTERACTION STUDIES AT HIGH REPETITION RATES

A new class of high-repetition rate (HRR) Peta-Watt-class (PW) laser systems make it possible to study laser matter interaction processes, like laser ion acceleration (LIA) and laser plasma instabilities (LPI), at unprecedented rates. These systems have the potential to generate immense amounts of data through rapid multivariable parameters scans of laser energy, pulse shape, spot size and others, in order to better diagnose and characterize the conditions underlying LPI and LIA.

However, detection media, typically image plates, film, CR-39, presently limits the repetition rate at which data can be collected from these systems. Rep-rated diagnostics are being redesigned to match the capabilities of current multi-Hz present and near future, PW-class laser systems. Here we present the development of a compact Thomson Parabola Ion Spectrometer capable of characterizing various ion species of multi-MeV ion beams from $> 10^{20}$ W/cm^2 laser produced plasmas at rates commensurate with the laser operation rates. This diagnostic makes use of a Polyvinyltoluene (PVT) based fast plastic scintillator (EJ-260), where the emitted light is collected by an optical imaging system coupled to a thermoelectrically cooled scientific complementary metal–oxide–semiconductor (sCMOS) camera. This offers a robust solution for data acquisition at HRR while avoiding the added complications and non-linearities of microchannel plate (MCP) based systems. Different ion energy ranges can be probed using the modular magnet setup, variable electric field, and a varying drift-distance. We have demonstrated operation and data collection with this system at up to 0.2 Hz from plasmas created by irradiating a solid target, limited only by the motorized target motion system. With the appropriate software and the use of machine learning techniques, on-the-fly ion spectral analysis will be possible, enabling real-time experimental con-

trol. The diagnostic design, calibration, and results from experiments at the ALEPH laser facility at Colorado State University (CSU) are presented.

In addition, we describe the results of the development of a novel scheme for the generation of spike trains of uneven delay (STUD) laser pulses using an array of hexagonal mirrors. By individually driving the offset of each mirror segment, we can divide the wavefront of the laser creating a pulse train of arbitrary delay. This pulse-train forming device can be used to conduct experiments related to a proposed method of mitigating the effects of LPI for inertial confinement fusion (ICF). By periodically turning on and off the laser drive of the ICF process, it has been postulated that the growth of parametric instabilities can be mitigated by allowing damping during the off-cycle of the STUD pulses. The use of the pulse-train forming scheme demonstrated here will allow us to study the effects of pulse train delay and duration best suited to LPI mitigation.

TABLE OF CONTENTS

LIST OF FIGURES

Chapter 1

Introduction

1.1 Motivation

Ultrashort high-intensity peta-watt (PW) class lasers [3,4] have emerged as promising tools for the study and generation of high energy density plasmas. These sources not only provide insight into different astrophysical phenomena like stellar cores and supernovas, but they also act as very practical tools for x-ray generation, particle acceleration, and as a potential energy source.

The primary example of this hypothetical laser driven energy source is inertial confinement fusion (ICF). This is a fusion process based on ablative compression of a fuel pellet. A laser incident on the ablative shell of a target pellet compresses the fuel enough to where it becomes hot and dense enough for the atoms in the core to fuse, releasing immense amounts of energy. This process is a hypothetical source of limitless clean fusion energy. Before this can be realized, issues plaguing the performance of ICF, like laser plasma instabilities, must be properly understood and controlled.

Alternatively, these laser systems are promising sources of accelerated protons and heavier ions. Most modern hadron accelerators rely on ring or linear RF accelerators which are extremely expensive and time consuming projects costing on the order of billions of dollars. Laser produced accelerated protons are encouraging sources for an inexpensive and compact injector for larger RF linear accelerators, energetic ions for hadron therapy, proton fast ignition, proton probing among a myriad of other applications.

Studies on the conditions required to optimize processes like laser ion acceleration and to mitigate effects like laser plasma instabilities are becoming increasingly important and necessary as the scientific community seeks to integrate these technologies into real-world systems. A new class of high repetition rate PW class lasers are opening the door to large, rapid, multivariate parameter scans to study the conditions underlying phenomena such as laser ion acceleration and laser plasma

instabilities. Instruments which aid the generation of these conditions as well as the diagnostics that resolve what occur during the laser matter interaction are being developed for high repetition rate operation to make these parameter scans possible. The design and results of two of these instruments are the focus of this thesis and are discussed in detail in the following chapters. Cursory information describing the laser matter interaction relevant to the tools developed is detailed below.

1.2 Particle Acceleration in Plasmas

As an electromagnetic wave propagates through the plasma, the ions remain immobile due to their large mass while the electrons are able to respond to the laser electric field. The immobile ion background will generate a restoring electric field which. the accelerated electrons will respond to the restoring force and oscillate at what is known as the plasma frequency given as

$$\omega_p = \sqrt{\frac{n_e e^2}{m_e \gamma \epsilon_0}} \tag{1.1}$$

Where n_e is the electron density, e is the elementary charge, m_e is the electron rest mass, $\gamma = 1/\sqrt{1-(v^2/c^2)}$ is the relativistic Lorentz factor and ϵ_0 is the permittivity of free space. An electromagnetic wave in this plasma will propagate according to Maxwell's equations with the dispersion relation

$$\omega = \omega_p + k^2 c^2 \tag{1.2}$$

When the laser wavelength $\omega_L > \omega_p$ the laser will propagate through the plasma with the following refractive index

$$n_p = \sqrt{1 - \frac{\omega_p^2}{\omega_L^2}} \tag{1.3}$$

When $\omega_L < \omega_p$ the plasma is described as overdense and the refractive index becomes imaginary and the laser will penetrate and evanescently decay to a distance of $l = \frac{c}{\omega_p}$, known as the colli-

sionless skin depth. The plasma is considered overdense for electron densities greater than some critical electron density that can be written as

$$n_c = \frac{m_e \epsilon_0 \omega_L}{e^2} \tag{1.4}$$

As the electron velocities begin to approach c, γ becomes non-negligible. In this case the electrons will have and effective mass greater than their rest mass. As a result ω_p effectively decreases resulting in a higher critical density for which the laser light of frequency ω_L can propagate in a phenomenon know as relativistic transparency.

1.2.1 Electron Motion and Heating

The details of the many mechanisms of hot electron generation and transport is beyond the scope of this thesis, however their generation and interaction in the plasma is fundamental to the understanding of the processes of MeV ion generation. So, they warrant a brief introduction.

For an incident plane wave with field values given by

$$\begin{aligned} \vec{E} &= E_0 e^{-i(\omega_L t - kz)} \hat{x} \\ \vec{B} &= B_0 e^{-i(\omega_L t - kz)} \hat{y} \end{aligned} \tag{1.5}$$

Where E_0 B_0 are the slowly varying field amplitudes. An electron placed in the plane wave will experience the Lorentz force defined as

$$\vec{F} = q(\vec{E} + \vec{v} \times \vec{B}) \tag{1.6}$$

when the dimensionless electric field amplitude $a_0 \equiv \frac{eE_0}{m_e \omega_L c} \ll 1$ the electrons are considered non-relativistic. The electron will oscillate in the field at a velocity know as the quiver velocity

$$v_x = \frac{eE_0}{m_e \omega_L} \tag{1.7}$$

In the cases where $a_0 > 1$ the $v \times \vec{B}$ component of Equation 1.6 becomes non-negligible and the electrons will drift along the laser axis with a velocity

$$v_z = \frac{a_0^2}{4 + a_0^2} c\hat{z} \tag{1.8}$$

We can note that for both scenarios the electron velocity depends on the applied electric field and at no point gains energy. Once the plane wave is turned off, the electrons will stop moving. In order to see how the electrons would gain energy in the laser field, we need to consider a more realistic scenario since an infinite plane wave is more of a mathematical construct. Typical laser setups involve a focused laser pulse whose intensity varies both spatially and temporally. If we think of a tightly focused beam with a Gaussian focal spot intensity profile, an electron initially in the center of the focal spot will see the highest intensity anywhere in the laser pulse. In the first half of the laser cycle the electron will be accelerated away from the center of the focus along the electric field lines toward the lower intensity region. During the second half of the laser cycle the electron will accelerate back toward the central focal spot, only that now, since it is in the lower intensity region, will not be able to return to its original position. This results in a net gain of kinetic energy for the electron away from the region of highest intensity. The cycle averaged resulting force of this effect is known as the ponderomotive force and can be written, for the non-relativistic case, as

$$F_{NR\_pond} = -\frac{e^2}{4 m_e \omega_L^2} \nabla (E \cdot E^*) \tag{1.9}$$

For the relativistic case the cycle averaged ponderomotive force becomes

$$F_{NR\_pond} = -m_e c^2 \nabla \gamma \tag{1.10}$$

The final electron energy will be given as

$$\Delta U = m_e c^2 (\gamma - 1) \tag{1.11}$$

As the photons are absorbed into the plasma, conservation of momentum shows that some of the electrons must be ejected along the laser propagation axis according to

$$p_{\parallel} = -m_e c(\gamma - 1) \tag{1.12}$$

Where Gibbon et al. [5] gives the relationship between $p_{\parallel}$ and $p_{\perp}$ as

$$p_{\parallel} = \frac{p_{\perp}^2}{2m_e c} \tag{1.13}$$

It's clear that the electron emission angle will be given by

$$\tan(\theta) = \frac{p_{\perp}}{p_{\parallel}} = \sqrt{\frac{2}{\gamma - 1}} \tag{1.14}$$

From this we can gather that as γ increases, the emission of accelerated electrons lies closer and closer to the laser axis.

There exists a variety of other mechanism by which laser light is able to couple to hot electrons. Resonance absorption occurs for obliquely incident light where the electric field is parallel to the density gradient (p-polarization). In this obliquely incident scenario the light will continuously refract throughout the underdense plasma according to Equation 1.3. The electron density to which the laser will propagate is at $n_e = n_c \cos(\theta_i)^2$ as opposed to n_c. The light will evanescently decay to the critical density where it resonantly excites plasma waves in the over-dense plasma. However, this heating mechanism is typically restricted to lower intensities due to the requirement of a longer scale length and shallow density profile.

More typical in ultra-intense laser matter interactions is the situation where the incident laser light causes profile steepening of the density gradient due to radiation pressure, a mechanical force exerted on the plasma as a result of conservation of momentum as the plasma absorbs, transmits and reflects incident laser radiation. From here electrons are ripped from the plasma accelerated in the laser field and ejected beyond the critical density into the over-dense plasma where the light will

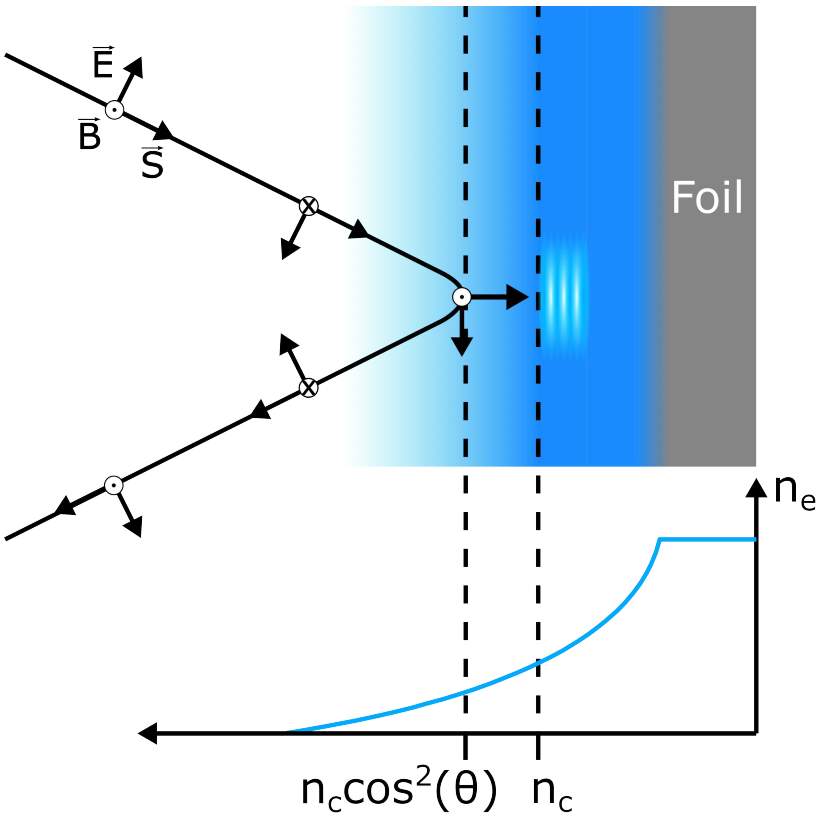

Figure 1.1: Illustration of resonance absorption where $\vec{E}$ denotes the laser electric field, $\vec{B}$ the magnetic field, and $\vec{S}$ the Poynting vector. The laser will refract through the plasma to an electron density of $n_e = n_c \cos(\theta_i)^2$. The electric field parallel to the density gradient will evanescently decay to the critical density where it can resonantly excite electron plasma waves in the plasma.

no longer effect them. this results in a net gain of energy on the electrons from their acceleration in the vacuum and is called vacuum heating [6].

For relativistic scenarios, J$\times$B heating arises from a high frequency 2omega component of the ponderomotive force [7] . This longitudinal oscillation leads to a non-resonant heating for intense laser pulses in a manner similar to vacuum heating and is more prominent for normal incidence beams [7].

Bremsstrahlung refers to the process by which an electron and ion undergo a Coulomb collision where the electron loses energy. Via conservation of energy, a photon is emitted corresponding to the energy lost by the electron. The inverse of the process is known as inverse bremsstrahlung, by which an electron collides with an ion and absorbs a photon, gaining energy in the process [8]. The collision frequency can be written as $\nu_{ei} = n_i \sigma_{ei} v_e$, where n_i is the ion density, σ_{ei} is cross-

section for electron ion collisions, and v_e is the electron velocity. This heating mechanism is more prominent at lower intensities ($< 10^{18}$ W/cm^2) due to the higher collisional cross-section at lower electron velocities though it is important for the coupling of the pre-pulse to the plasma.

The hot electron energy distribution is described well enough by a Boltzmann distribution

$$n_{hot}(E) = n_0 e^{-\frac{E}{k_b T_{hot}}} \tag{1.15}$$

with the temperature scaling with the ponderomotive potential as described by Wilkes [9]

$$T_{hot} = m_e c^2 \left[\sqrt{1 + \frac{I\lambda_{\mu m}^2}{1.37 \times 10^{18}}} - 1 \right] \tag{1.16}$$

Alternate scalings include Beg [10], Pukhov [11], etc. and the scaling needed for any scenario de-

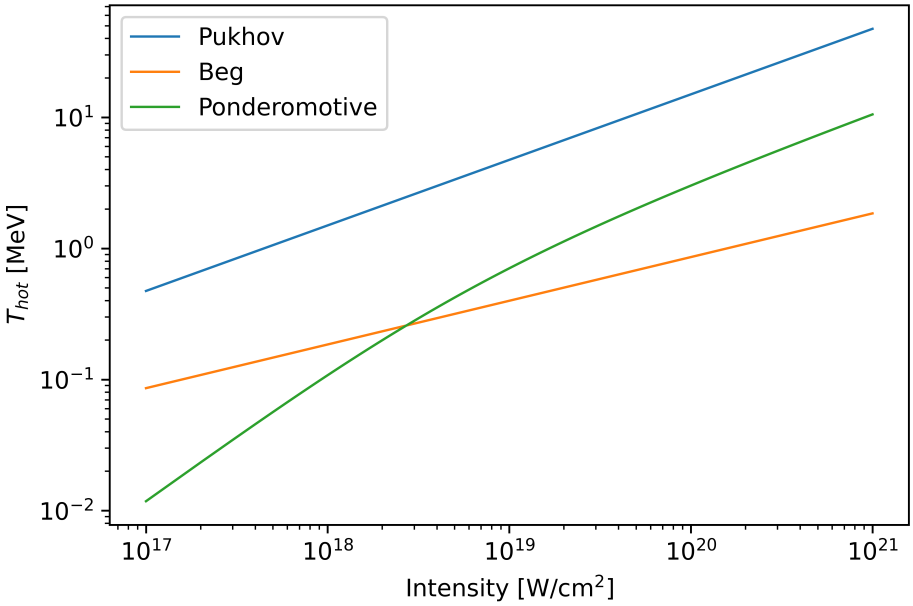

Figure 1.2: Comparison between different hot electron temperature scalings

pends strongly on laser intensity, pre-pulse duration, contrast, polarization, angle of incidence, etc. We can see in Figure 1.2 that there is significant disagreement between the different temperature

scalings at different intensities. This illustrates the motivation for the study of the scaling which best suits specific laser and target parameters.

1.2.2 Ion Acceleration

While the electrons are highly mobile in the laser field, as discussed above with the myriad of electrons acceleration and heating mechanisms, the ions are nearly immobile. The large mass of the ions compared to the electrons means the laser field has little direct effect on them. Directly accelerating ions in the forward direction to MeV energies would require intensities in excess of 10^{24} W/cm^2 [12] which is far beyond the capabilities of modern laser systems. One of the main mechanisms currently used for the acceleration of ions is known as target normal sheath acceleration (TNSA) [13]. TNSA provides a mechanism by which strongly beam-like bunches of ions are accelerated on the rear side of a solid target, normal to the surface of the target. Current experiments have yielded energies in excess of 100 MeV ions [14]. The interaction is quite complex, and the theory surrounding it is not yet fully developed. However, the process by which it occurs proceeds roughly as follows. As the laser pre-pulse impinges on the front side of the target, the atoms

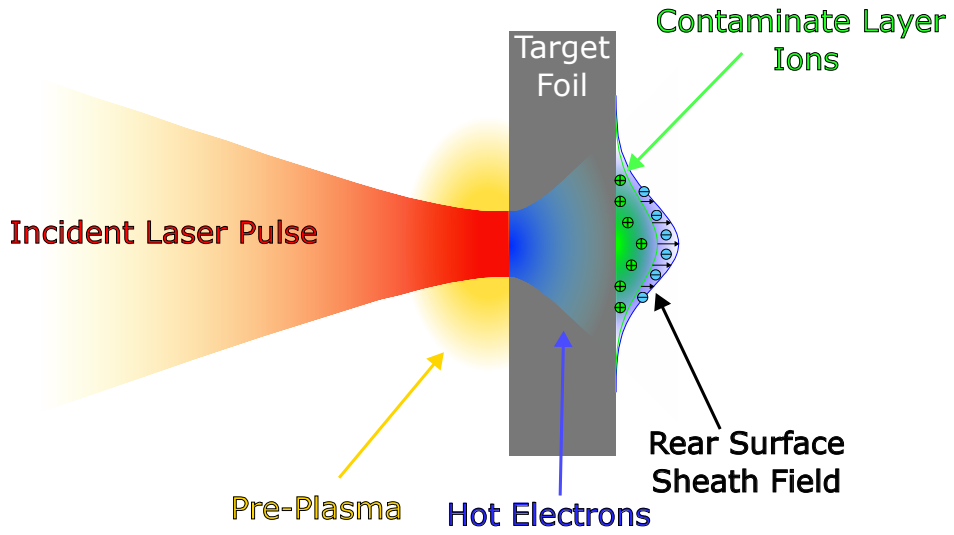

Figure 1.3: Illustration of the target normal sheath acceleration process. The incident laser pulse will couple energy to hot-electrons in the pre-plasma on the target front surface. The hot-electrons will transport through the bulk of the target, diverging in the process, and emerge on the rear side of target. This generates a sheath field with a contaminate layer of ions on the rear surface where protons and other heavier ions will be accelerated in the process.

begin to ionize forming a pre-plasma on the front surface of the target. Via the various heating mechanisms described above, hot electrons are generated at the target front surface and transport through the bulk of the target. As the hot electrons emerge from the rear surface of the target and begin expanding in free-space, the electric field generated by the hot electron cloud ionize a contaminate layer of water and hydrocarbons on the target rear surface [15]. This strong sheath field between the hot electrons and the ionized contaminate ions accelerates the ions in rear surface target normal direction with beam-like divergence. Just as with the variety of electron scalings, there are a number of expansion models for ions. One such model is the plasma expansion model which is a quasi-neutral, isothermal fluid model. Fuchs [16] and Mora [17] are a couple of examples. Fuchs' model is a good predictive tool based on varying laser and target parameters and scales the maximum proton energy by expanding on Mora's model.

$$E_{max} = 2T_{hot}[ln(t_p + (t_p^2 + 1)^{1/2})]^2 \tag{1.17}$$

Where $t_p = \frac{\omega_p t_{acc}}{\sqrt{2exp}}$ is the normalized acceleration time, ω_{pi} is the ion plasma frequency, t_{acc} is the effective acceleration time which Fuchs provides as $t_{acc} \approx 1.3\tau_{laser}$, and $n_{e,0}$ is the electron density driving the rear surface sheath field. The electron density driving the sheath field can be estimated first with the total number of electrons driving the expansion $N_e = fE_{laser}/T_{hot}$, where f is the fraction of the laser light coupled to the pre-plasma which scales as $f = 1.2 \times 10^{-15} I^{0.74}[W/cm^2]$. These electrons will spread through the target of thickness d and with and angular divergence of θ to a sheath surface of area $S_{sheath} = \pi(r_0 + d \times tan(\theta))^2$ and will give a density of $n_{e,0} = N_e(c\tau_{laser} S_{sheath})$, where r is the laser spot size. We can note that $E_{max} \propto T_{Hot}$ which means the maximum ion energy roughly scales with $\sqrt{I}$. Other mechanisms of acceleration have been studied including radiation pressure acceleration [18, 19], Coulomb explosion acceleration [20], laser break-out afterburner [21], etc. However at ultra-high laser intensities [22] and micron scale target thicknesses [23], TNSA often dominates.

1.3 Colorado State University ALEPH Laser System

The laser at CSU [24] is a chirped pulse amplification (CPA) [3] based Ti:Sapphire laser. With a center wavelength of $\lambda_0 = 800$ nm and a bandwidth of about $\Delta\lambda = 50nm$ FWHM. A Kerr-cell mode-locked oscillator operating at a frequency of 86 MHz generates a pulse train seed for the laser. The pulses are broadened to 550 ps with a grating stretcher and the 86 MHz pulses are down selected with a Pockels cell to 10 Hz. The pulses go through 5 stages of amplification. The first two are pumped by a commercially available Quanta-Ray Pro 270, frequency doubled, Q-switched, Nd:YAG laser with an output of 600 mJ at 10 Hz. The following 3 stages are pumped by a set of in-house designed Nd:Glass slab amplifiers pumped by Xe flashlamps, capable of firing at up to 3.3 Hz. The slab amplifiers received seed light from a chain of Nd:YLF rod amplifiers fed by a

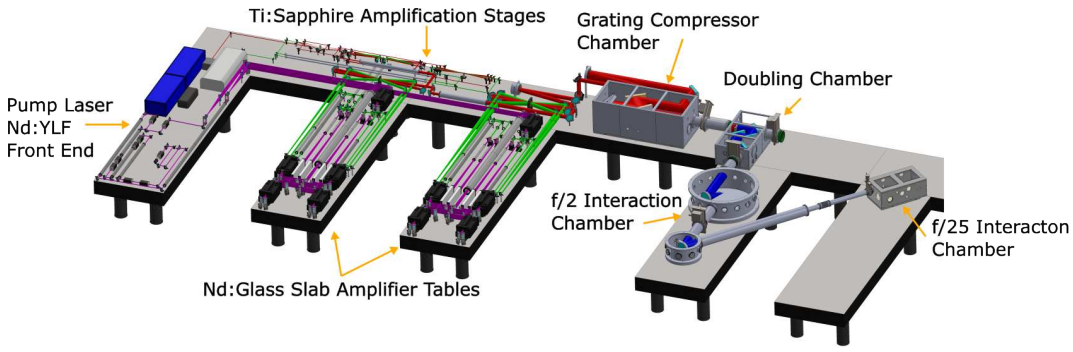

Figure 1.4: Overview of CSU ALEPH Peta-Watt Laser System

Q-switched Nd:YLF oscillator. After the final amplification stage, the 36.3 J beam's diameter is expanded to 185 mm and sent into the vacuum grating compressor. The pulse can be compressed to 30 fs. Accounting for the throughput of the compressor, we get a maximum pulse energy of about 25.4 J on target. This gives a peak power of 0.85 PW. The laser can operate in either its $\lambda_0 = 800$ nm fundamental wavelength or at its $\lambda_0 = 400$ nm second harmonic. The fundamental beamline consists of a single turning mirror into the interaction chamber. In the nanosecond range the contrast of the laser system is measured to be 10^8. The second beamline is a high-contrast second harmonic beamline where the 800 nm pulse is frequency doubled using an 800 μm thick KDP crystal with conversion efficiencies of $> 40\%$ readily achievable. The remaining fundamental

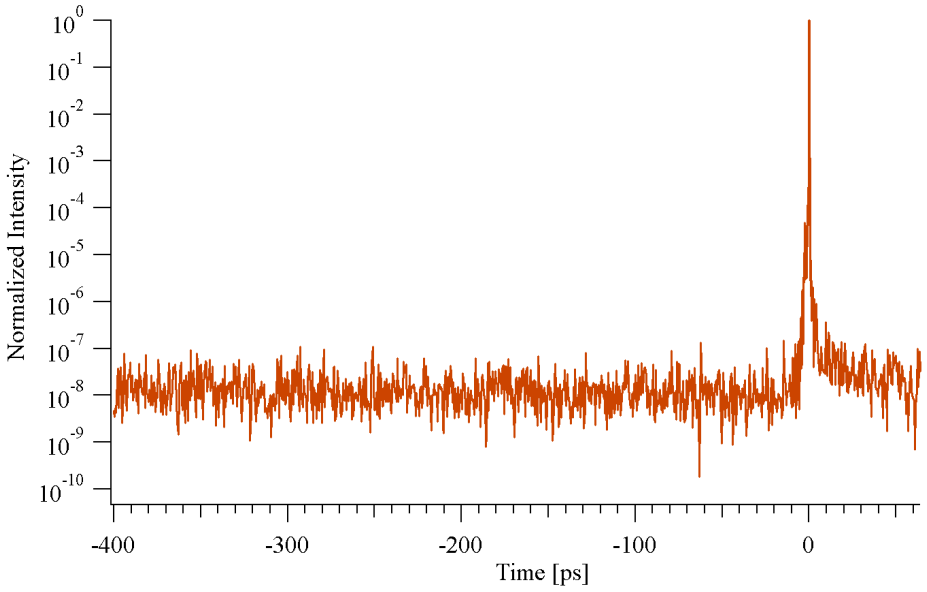

Figure 1.5: Third order cross-correlation (SEQUOIA) measurement of the fundamental pre-pulse contrast

light is filtered using a sequence of five dichroic mirrors. The second harmonic generation process improves the contrast to $> 10^{12}$

Chapter 2

Thomson Parabola Ion Spectrometer

This ability to produce yields of high energy protons shows promise as a technology as a compact injector to hadron accelerators, proton probing experiments, hadron therapy, etc. It is important to improve the conditions by which you can either increase the maximum energy and yield of ions. There is promise with current laser systems that generate these energetic ion sources at rates never thought possible with the systems from some of the earliest ion sources. The high repetition rate laser system show the potential to generate extremely large data sets from multivariate parameter scans of laser energy, pulse shape, spot size in order to better diagnose and characterize MeV particle acceleration conditions. While many modern ultra high-power laser systems are capable of the repetition rate required to generate these large data sets, the plasma diagnostics that resolve what occurs in these plasmas have not evolved with their sources.

Columbia Resin 39 (CR-39) is a solid-state nuclear track detector used for the detection of ionizing radiation. As ionizing radiation travels through the material, it leaves behind a trail of damaged polymer bonds in the plastic due to the energy deposited in the plastic structure [25, 26]. The detector is then etched in a $NaOH$ solution where the tracks, or "pits" as they are typically referred to as, etch away faster than the undamaged plate. This allows the user to observe the pits created from the ionizing particles. Different types of radiation and even different ion species being observed will create characteristic pits with specific depth of deposition, diameter, shape, etc. This detection media is quite versatile and detailed in its ability to distinguish between different ion species and radiation types. However, it suffers from the fact that is is impossible to operate at high repetition rates. The plates need to be removed from the vacuum system, whether venting the whole target chamber or a smaller external chamber, which itself can take 10's of minutes to an hour or more depending on the size of the chamber and location of the detector plate. An even larger impediment to the operation rate of CR-39 is the etching process which can typically take hours to both etch and record the results.

Image plate is another ubiquitous detection medium used in energetic particle diagnostics. This mechanism of detection relies on the dopant Eu^{2+} losing an additional electron due to energy deposition from ionizing radiation [27]. This free electron then becomes bound to either FBr or FI and enters a metastable state. With the excitation of the now FBr^{-} or FI^{-} with a 620 nm laser, the electron recombines with the Eu^{3+} ion and emits a 413 nm photon. This process is know as photostimulated luminescence (PSL). The detector is typically raster scanned in commercially available IP scanners in which the emitted signal light is collected by a photomultiplier tube (PMT) internal to the scanner and the signal recorded vs position in the scanner. This scanning process can take several minutes depending on the size of the image plate sheet. This is in addition to the vacuum venting cycles needed in order retrieve the detector, similar to the CR-39.

Micro-channel Plates (MCP) offer an option to retrieve data at a high rate, however these require high vacuum, are expensive, and are prone to damage. MCP's also gain scales strongly with the applied voltage, making the retrieval of absolute ion number difficult.

In this chapter, we present the design of a Thomson parabola ion spectrometer that makes use of a plastic organic scintillator based on Polyvinyl toluene (PVT) to act as a detection medium from which we can gather large data sets at a high repetition rate (HRR), representing data collection increases of $> 10000\times$ compared to typical shot per hour experiments.

2.1 Thomson Parabola Ion Spectrometer Design

2.1.1 Thomson Parabola Basics

The Thomson Parabola Ion Spectrometer (TP) is a simple and ingenious diagnostic that has been around for over a century [28] and is a staple in the field for spectrally resolving various ion species. In its most basic form, a Thomson Parabola Ion Spectrometer consists of a parallel electric and magnetic fields. As a charged particle passes through the apparatus it experiences the Lorenz force seen in Equation 1.6. Setting up a system of coordinates, we say the ion will travel in the $+\hat{z}$ direction and the magnetic and electric fields are both in the $+\hat{x}$. While in the magnetic field the ions will see the $\vec{F} = q\vec{v} \times \vec{B}$ component of the Lorentz force and will be swept in the $+\hat{y}$ direction

with the corresponding Larmor radius $r_l = \frac{m\vec{v_\perp}}{|q|\vec{B}}$ where m is the ion mass, $\vec{v_\perp}$ is the ion velocity normal to the B-field, q is the charge of the ion, and $\vec{B}$ is the magnetic field. Since the incoming velocity of the ion through the pinhole is in the $+\hat{z}$ $+\hat{z}$ the ions initial velocity to $\vec{v_\perp}$. After passing through the magnetic field they will propagate with an angle θ with respect to the $\hat{z}$ axis given by the equation.

$$tan(\theta) = \frac{L_B}{\sqrt{r_l^2 - L_B^2}} \tag{2.1}$$

The overall $\hat{y}$ dispersion will be both the dispersion from the drift after exiting the magnets as well as that accumulated in the field. This will be given by,

$$y_{disp} = r_l - \sqrt{r_l^2 - L_B^2} + D_B tan(\theta) \tag{2.2}$$

Where L_B is the length of the magnets and D_B is the drift length from the rear side of the magnets to the detection plane. Assuming $L_B \ll r_l$ this shortens to

$$y_{disp} \approx \frac{L_B(D_B + \frac{L_B}{2})}{r_l} = \frac{qBL_B(D_B + \frac{L_B}{2})}{\sqrt{2mE_{kin}}} \tag{2.3}$$

From this we gather that the $y_{disp} \propto \frac{1}{\sqrt{E_{kin}}}$. Where E_{kin} is the ions kinetic energy. Similarly for the electric field, the ions will accelerate in the $+\hat{x}$ direction along the electric field lines. Note, this sweep in the $+\hat{x}$ direction is parallel to the B-field of the magnets and thus this deflection will not affect the dispersion in the $+\hat{y}$ direction at the detector plane. This is important so as to preserve the spectral information of the ions. After exiting the field of the electrodes, the ions will propagate to the detector plane with an angle ϕ which can be given by,

$$tan(\phi) = \frac{qEL_E}{2E_{kin}} \tag{2.4}$$

And the total drift of the ions at the detector plane will be

$$x_{disp} = \frac{qEL_E^2}{4E_{kin}} + tan(\theta)D_E = \frac{qEL_E}{2E_{kin}}(D_E + \frac{L_E}{2}) \tag{2.5}$$

Making a few assumptions: $L_E = L_B = L$, $D_E = D_B = D$, $D \gg L$, we get

$$y_{disp}^2 = \frac{q}{m}\frac{B^2LD}{E}x_{disp} \tag{2.6}$$

For an applied electric field E, magnetic field B, field length L, and drift length D our ions will be sorted into discrete parabolas based on the charge-to-mass ratio $\frac{q}{m}$. This can act as a good first order calculation of the dispersion. Unfortunately, it does not take into account the designs of many current TP's. Many of which make use of different electric and magnetic field lengths as well as arbitrary field plate geometries. One has to make a choice between the ease of calculation of the ion dispersion, and more practical consideration for the diagnostic itself in terms of compactness, spectral range of interest, etc.

2.1.2 Thomson Parabola Design

The Thomson parabola consists of a collimating pinhole, ((a) in Fig 2.1)) a deflection region containing permanent magnets (b) and a biased electrode pair (c), an alignment back pinhole (d), and a detector (e). In order to retrieve an ion spectrogram we require a collimated beam of ions. The collimation of the ion beam was achieved by a brass pinhole. Brass was chosen due to its relatively high density, easy machinability and because it is non-magnetic. This limits any fringing magnetic field at the pinhole. Pinholes were machined with 150 μm, 300 μm, and 680 μm diameter hole versions available. The pinhole selection sets the spectral resolution of the instrument. The pinhole was placed into a tight tolerance recessed hole in a thick aluminum shielding front wall. This wall limits any other charged particles not collimated by the pinhole , and reduces any background x-ray signal. After collimation the ions travel through the magnetic and electric fields and begin to deflect. As seen previously, a main characteristic of a TP is the ability to separate

different ion species by their charge to mass ratio. There are a few instrument parameters that can be optimized in order to improve performance, especially for higher energy ions where different species are more likely to overlap. In increase the electric field the field plates can be placed closer together, or the voltage can be turned up. Both have major drawbacks as placing the plates too close limits the lower energy spectrum that can be resolved as the ions start to collide with the field plates during propagation. Turning the voltage up also has the drawback of increasing the likelihood of arcing. A solution that has been used before [29–31] is to use a wedge plate configuration. This scheme allows for high electric field at the beginning of propagation while allowing for the lower energy ions to disperse while avoiding spectral clipping. The position and the angle of the field plates we set by a machined Teflon plastic holder. Teflon was chosen for its high dielectric strength, $\sim 19.7\frac{kV}{mm}$, and good vacuum properties. The distance between the field plates was selected to increase from 2 mm to 22 mm. The length of each electrode L_E is 150 mm. The Teflon was recessed from the minimum plate separation to avoid arcing across the surface aided by contaminates or sharp features that may lead to field enhancement. The high voltage connection to the plate is made with grounded and shielded high voltage (SHV) cables. The magnetic field was designed with consideration of the fact that different ion spectral region of interest will be probed depending on the experiment being performed. This means that, barring changing the drift length of the ions after deflection, we would need to be able to change the magnetic field itself. One advantage of using something like an electromagnet when operating a Thomson parabola is the ability to change the field strength by simply varying the voltage/current. However, this design presents its own issues including the propensity to overheat in vacuum, necessitating the use of pulsed excitation [32] or water cooling. To avoid the complications associated with running an electromagnet based TP, we opted for a modular permanent magnet design. In our design the magnets sit in a pair of removable aluminum holders that can be easily changed allowing us to insert magnets of varying strength. We used two commercially available neodymium magnets $50.8 \times 50.8 \times 12.7$ mm in size from KJ Magnetics. with a nominal surface field of 0.27 T. The previous model of TP in use at CSU was external to the chamber. It was mounted on a flange at a

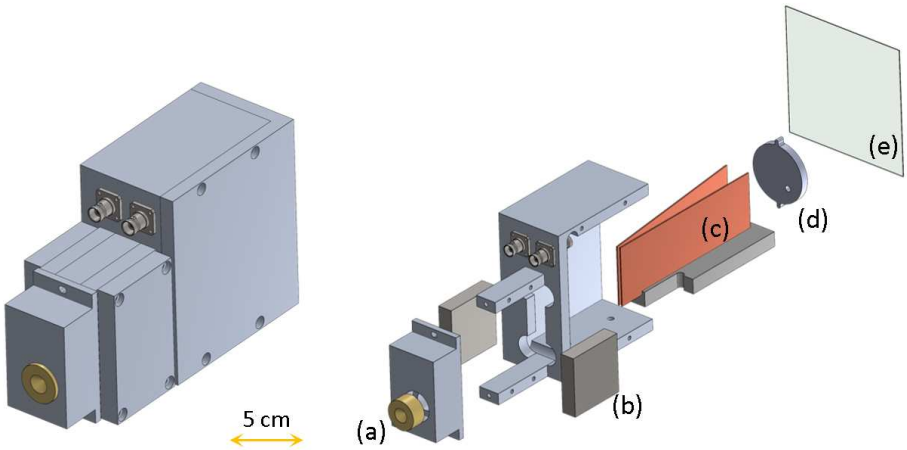

Figure 2.1: Exploded view of the Thomson parabola spectrometer: (a) Pinhole, (b) Magnets, (c) Wedge electrodes, (d) rear alignment pinhole, (e) detection media

half meter from the target. This setup results in an extremely small solid angle of collection, thus requiring the use of an microchannel-plate intensifier (MCP). In order to ensure our scintillator creates enough photons for a visible camera to see without the use of an intensifier, the spectrometer's pinhole sits as close to the source as necessary for sufficient signal on the scintillator. Also, in order to operate in an ordinary experimental configuration, where the TP is used in conjunction with a multitude of other instruments, the TP was designed to be compact. We designed the front of the instrument to not exceed a length of 45 mm and the rear of the instrument to not exceed a length of 70 mm. The main body of the TP was machined out of a single block of aluminum. This kept the instrument as monolithic as possible.

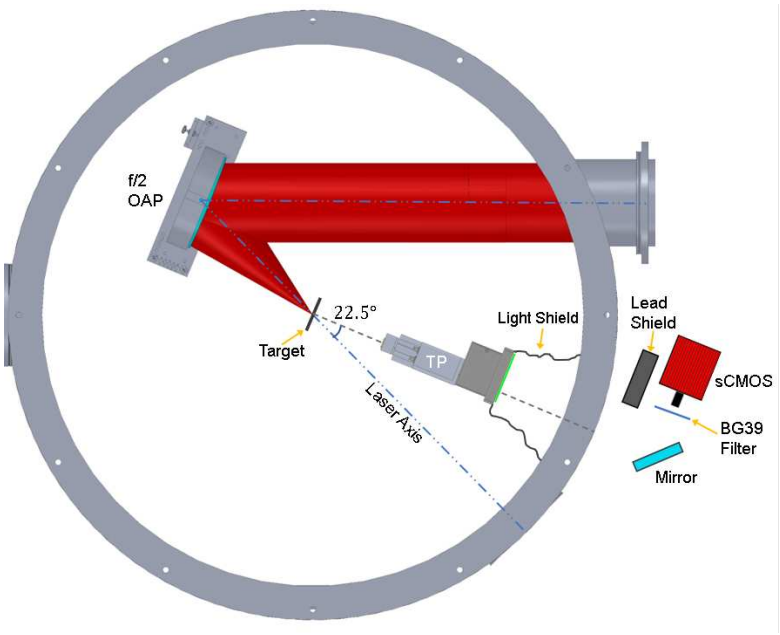

Figure 2.2: Calibration experimental layout of the spectrometer in the f/2 configuration at the fundamental frequency

2.2 Characterization

2.2.1 Simulation

The analytic formula for the dispersion seen in Equations 2.3 and 2.5 are for an ideal Thomson parbaola with parallel magnets and electrodes. As discussed in the previous section we opted for a wedge electrode arraignment for the instrument to accommodate the sweep of lower energy ions. Because of this, a simulation script was written in Python [33] to obtain a first order approximation of the dispersion from our setup. The script acted as an ion tracking software where ions of a specified energy range were initialized each with a position and velocity matrix.

$$\vec{r} = \begin{bmatrix} x \\ y \\ z \end{bmatrix}, \quad \vec{v} = \begin{bmatrix} v_x \\ v_y \\ v_z \end{bmatrix} \tag{2.7}$$

Here z is the direction of propagation, x is the direction of the fields, and y is the energy dispersion direction. The velocity matrix is initialized to have just a $+\hat{z}$ component corresponding to the

kinetic energy of each of the ions. The electric field dispersion was calculated using the time of flight of the particles, $\Delta v_x = \frac{qE\,dz}{m_i v_z}$, where q is the ion charge, E is the electric field, dz is the step size, and m_i is the ion mass. As the ions are stepped through the B-field, there is rotation matrix applied to velocity vector.

$$R = \begin{bmatrix} 1 & 0 & 0 \\ 0 & cos(\theta) & -sin(\theta) \\ 0 & sin(\theta) & cos(\theta) \end{bmatrix} \tag{2.8}$$

The angle of rotation is related to the θ from the theoretical dispersion $\theta = arctan\left(\frac{dz}{\sqrt{r_l^2 - dz^2}}\right)$ where dz is the step size and r_l is the Larmor radius. The electric field used for the simulation was obtained as a 2-D Vector field inside the wedge plates using the Laplace equation.

$$\nabla^2 V = \frac{1}{r}\frac{d}{dr}\left(r\frac{dV}{dr}\right) + \frac{1}{r^2}\frac{d^2V}{d\phi^2} + \frac{d^2V}{dz} = \frac{1}{r^2}\frac{d^2V}{d\phi^2} \tag{2.9}$$

Where the E field can be written as

$$E(r,\phi) = -\nabla V = \frac{V_0}{r\phi_0}\hat{\phi} \tag{2.10}$$

Or [30]

$$E_x(x,z) = \frac{zV}{(x^2+z^2)\phi_0}\hat{x}, \quad E_z(x,z) = -\frac{xV}{(x^2+z^2)\phi_0}\hat{z} \tag{2.11}$$

The $\hat{z}$ component of the electric field is relatively small compared to the $\hat{x}$ component, but it is a necessary addition for the fringing effect of the field. Without taking it into account, the dispersion of lower energy ions are slightly different than that of the real traces.

An empirical approach was taken for the magnetic field. A Hall probe was incrementally stepped along the path of the ions to record the field. To get an effective $\vec{B}$-field a second order

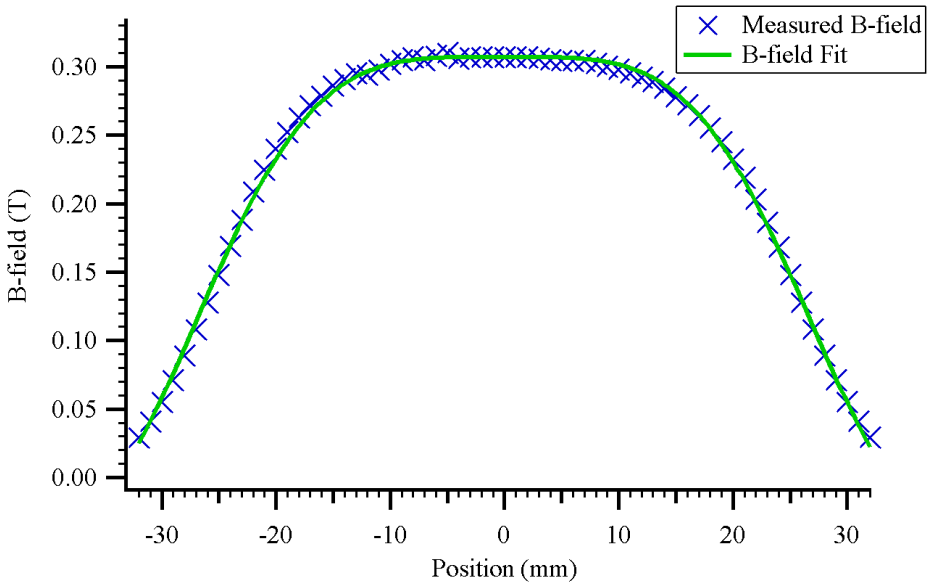

Figure 2.3: Measurement of B-field along ion path and corresponding super-gaussian fit

super-gaussian, $B(x) = Ae^{-\left[\frac{x}{width}\right]^4} + y_0$, was fit to the measured B-field data in Igor. An effective B-field was calculated according to the following equation

$$B_eff = \frac{1}{L_B} \int B(x)dx \tag{2.12}$$

Where L_B is the length of the magnet, and the length over which ions are dispersed in the simulation. This resulted in an effective B-field of 0.2907 T. The ions were stepped through the TP in fixed increments of length dz, and the x and y positions were stepped relative to dz based on the relative velocity of v_x and v_y to v_z. The ions continue to step through the instrument until they hit the detection plane where their x and y values were recorded.

Figure 2.4 shows an example trace at the detector plane. Plotted are a range of energies for protons, deuterons, and carbon 1-6+. Note, the overlap between the deuterium and carbon 6+ lines arises from their equivalent charge to mass ratio.

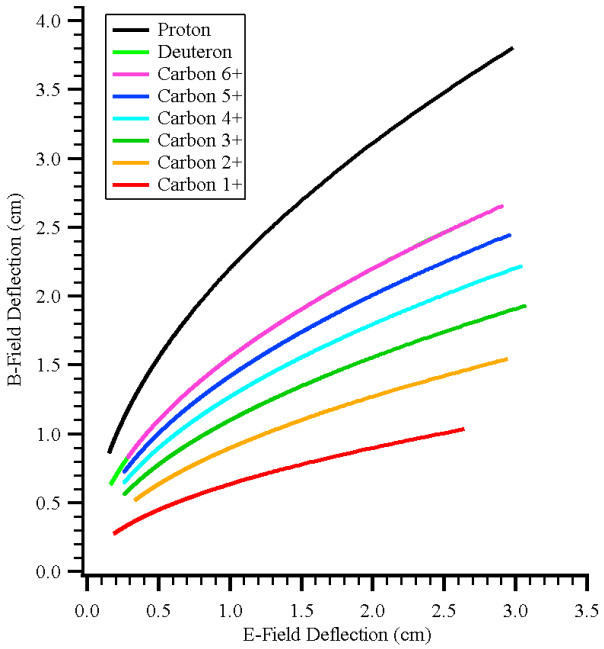

Figure 2.4: Simulation of traces for protons, deuterons, and carbon 1-6+ ions

2.2.2 Calibration

The stopping power of ions was calculated by Bethe in 1930 [34] using time-dependent perturbation theory as

$$-\frac{dE}{dx} = \frac{2\pi n z^2 e^4}{mv^2}\left[ln\left(\frac{2mv^2 W_{max}}{I^2(1-\beta^2)}\right) - 2\beta^2 - \delta - U\right] \tag{2.13}$$

Where $\beta = \frac{v}{c}$, v is the velocity of the particle, I is the mean excitation potential, n is the electron density, m is the electron mass, z is the charge of the particle, $W_{max} = \frac{2mv^2}{1-\beta^2}$is the maximum energy transfer in a single collision, δ is the density correction. U is the shell correction which takes into account the orbital motion of target electrons. Ions experience what is known as a Bragg peak. This arises from the small stopping power for higher energy ions that sharply increases as the energy decreases. This results in ions traveling through matter like metals or plastics, depositing little energy, but still enough energy to slow them down. The stopping power sharply increases as the energy of the particle decreases. This causes a positive feedback loop as the particle slows and the energy deposition increases resulting in a sharp spike in energy deposition as seen in Figure

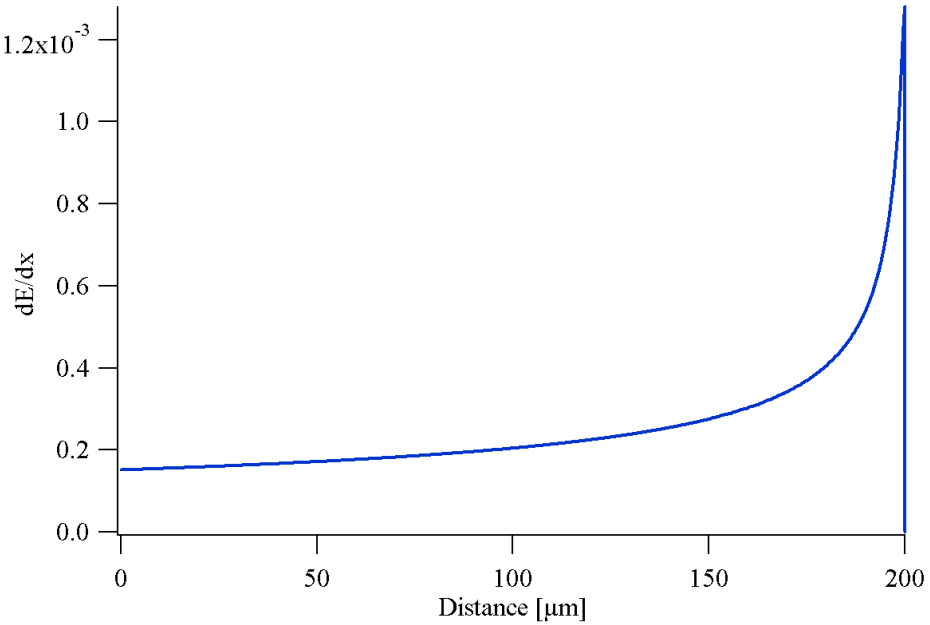

Figure 2.5: Example of energy deposition of 5.12 MeV protons through 200 μm of Al

2.5 for 5.12 MeV protons. This spike in energy deposition occurs at a specific depth beyond which the ion of a specified initial energy will not penetrate and before which the ions will nearly totally transmit. This fact is leveraged for the calibration of this diagnostic to avoid the most costly and time consuming approach of securing time at a linear accelerator facility [35]. If a filter made of something such as aluminum is placed in the path of a proton beam with a range of energies, there will be a definite cutoff energy that arises due to the Bragg peak of ions passing through the material. Specific cutoff energies can be calculated based on the filter thickness. We can use a series of filters of different thicknesses to obtain a series of cutoff energies. Placing the filter set at the detector plane allows us to obtain a calibration curve of the instrument's dispersion. A series of aluminum foils were used as the absorptive filters for the calibration with thicknesses of 4 μm, 10 μm, 25 μm, and 38.1 μm. FujiFilm BAS MS image plate was used as the detection media. We note that the MS image plate contains a 9 μm Mylar protective layer. In order to perform the ion cutoff energy calculation we used stopping power data from NIST's P-star database [36] for both aluminum and Mylar. The cutoff energy calculation was performed using a Python script where protons of different energies were iteratively stepped through the aluminum filter and Mylar

protective layer. The corresponding stopping power was used to calculate the energy lost in each iteration. The lowest energy proton that was able to transmit through the filters was recorded as the temporary cutoff energy. Corrections were made to account for the additional path length of material traversed by ions entering the filters with some angle θ which could be estimated analytically for the temporary cutoff energy by Equations 2.1 and 2.4. The new path length through each filter was taken as $l_{eff} = \frac{l_0}{\cos(\theta)}$. The cutoff energy calculation and corrections were repeated until the results converged to a final proton cutoff energy. Once the proton cutoff energy was calculated, data was collected by irradiated a solid 9 μm Al foil target. The results for this series of shots are show in Figure 2.6. The straight line corresponds to shots that were taken with no voltage applied to the electrodes and the parabolic traces correspond to protons for a 6 kV voltage applied to the electrodes. The x-ray/neutral spot, seen as the dot in Figure 2.6 and as the spike

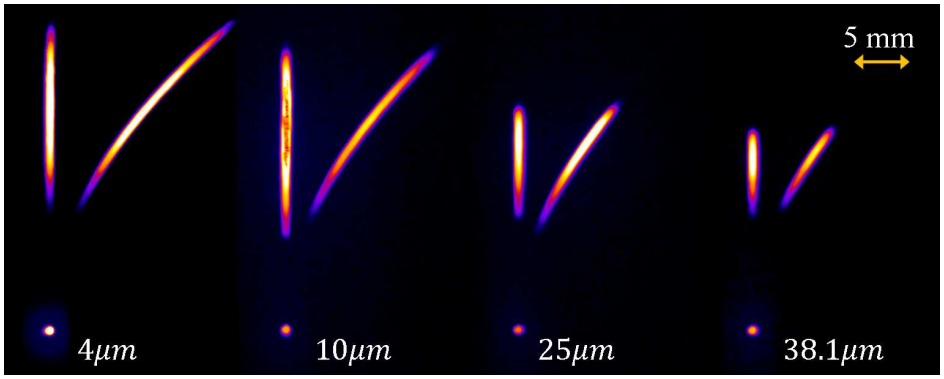

Figure 2.6: Raw images of calibration shots showing traces of protons for no applied voltage as well as $6kV$ voltage. The spot seen at the bottom of each image corresponds to the x-ray/neutral zero deflection position.

in the example lineout in Figure 2.7, was taken as the zero point. The distance to the signal cutoff was recorded for each filter thickness. Recalling from Equation 2.3, the magnetic deflection of ions $y_{disp} \propto \frac{1}{\sqrt{E}}$. The observed deflection distance was plotted vs $\frac{1}{\sqrt{E}}$. The calibration curve was obtained by applying a linear fit to the data. The resulting trace is shown in Figure 2.8 along with the simulated deflection for the same energies. As we can see, there is strong agreement between the calibrated and simulated deflection. This calibration was performed for protons only.

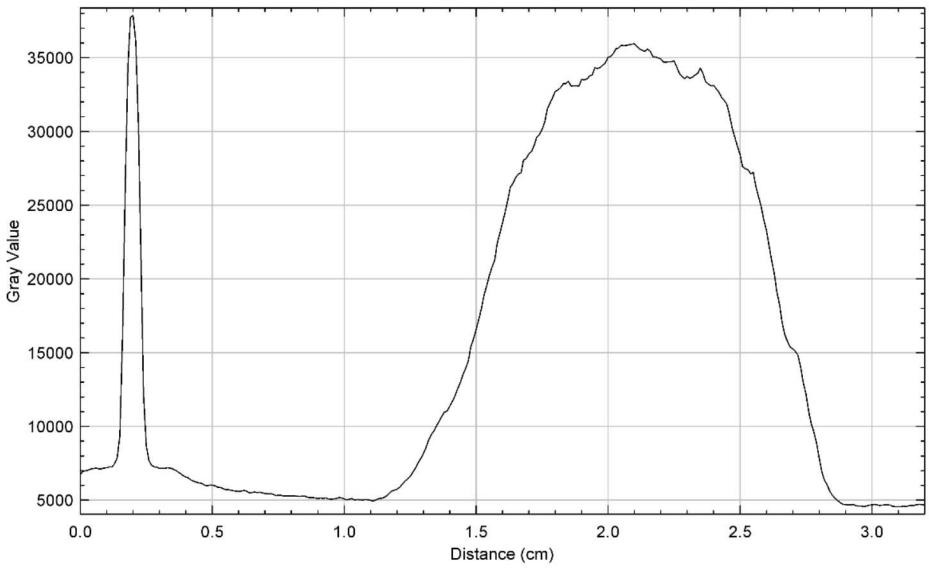

Figure 2.7: Example lineout of a proton trace used for determining deflection distance of energy cutoff. The spike on the left corresponds to the x-ray/neutral zero order.

A similar method to calibrate different species of heavier ions would be impractical due to the higher stopping power seen by these ions. The high stopping power would require the use of impractically thin filters to observe a low enough cutoff energy that could be generated in this experimental configuration. However, since we see strong agreement between the simulation and calibration for protons, the simulation data for heavier ion species could act as a good first order estimation of the dispersion relation.

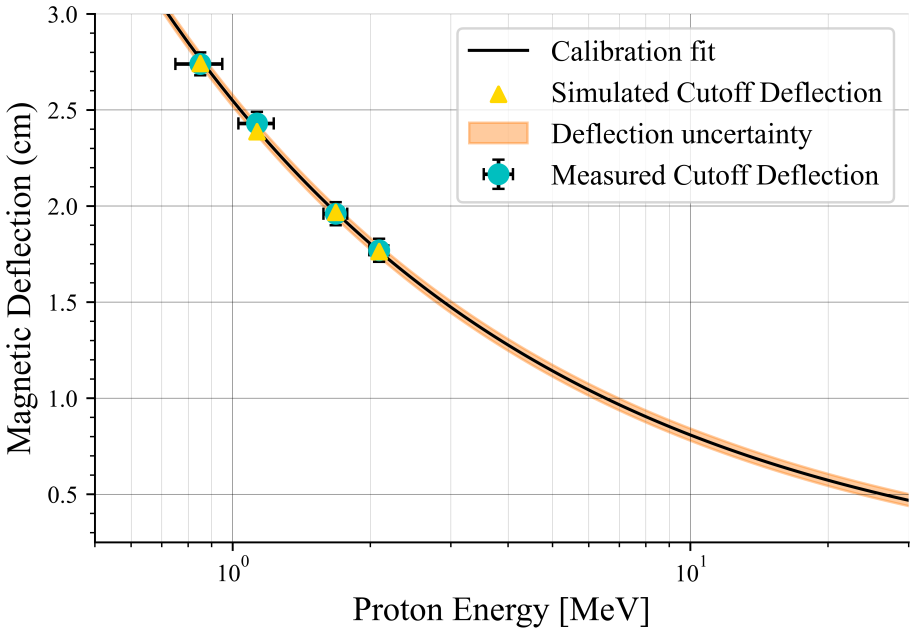

Figure 2.8: Calibration data showing both measured and simulated data points as well as the calibration curve fit.

2.3 Operation at High Repetition Rate

2.3.1 Scintillator Response and Spectrum Retrieval

In order to retrieve a meaningful spectrum from our scintillator shot results, we need some form of calibration or model for the spectral response of our scintillator for different ions. In 1951, Birks [37] proposed an empirical formula for the light yield from scintillators. It states that the light per unit distance emitted due to the energy deposition from radiation in a scintillator is a function of the energy deposited where the relation is given as

$$\frac{dL}{dx} = S\frac{\frac{dE}{dx}}{1 + k_B\frac{dE}{dx}} \tag{2.14}$$

For ions the equation describes a nonlinear response of the scintillator to the stopping power=. For low stopping powers, the light yield as a function of distance, $\frac{dL}{dx}$, is linearly related to the stopping power of the ions scaled by S, the scintillation efficiency. However, as the stopping power begins to increase, the emitted light begin to deviate from its linear response and saturates to a constant

value given by $\frac{S}{kB}$, where k_B is referred to as Birks' constant or the quenching factor. An example light yield vs stopping power plot for the organic scintillator Anthracene can be seen in Figure 2.9. The quenching effect is mainly dominated by ionization quenching in organic scintillators

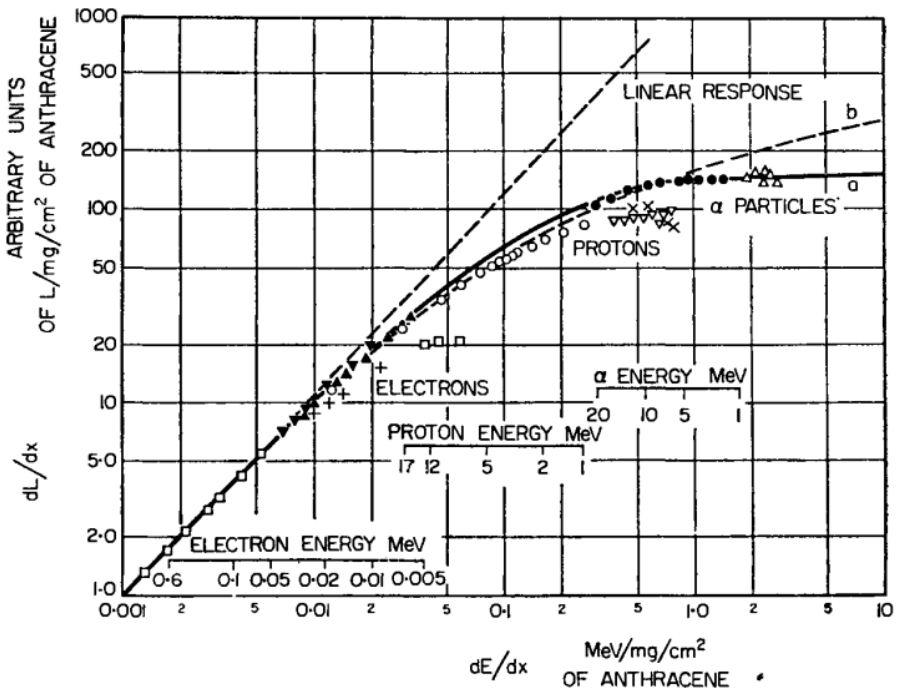

Figure 2.9: Nonlinear response of Anthracene showing saturation of light yield response as stopping power increases [1]

wherein ionizing radiation like ions leave a path of damaged or ionized molecules along its path of travel. These damaged or ionized molecules act to capture excitons and decay non-radiatively. The excitons would otherwise transfer energy to the scintillating molecule and emit light.

There are two main experimental methods for the determination of light yield as a function of ion energy [38]. The direct method is to bombard the scintillating material directly with well-characterized charged particles like ions and measure the response. The indirect method is to bombard a scattering source with neutral radiation like gamma rays or neutrons and use a unique angle to select the energy of the scattered charged particles on the scintillator an to measure the response. This indirect neutron scatter technique was used by Awe et al. [39] to retrieve the quenching factors of protons for the green-shifted PVT based scintillator, EJ-260. An additional non-linear term k_C

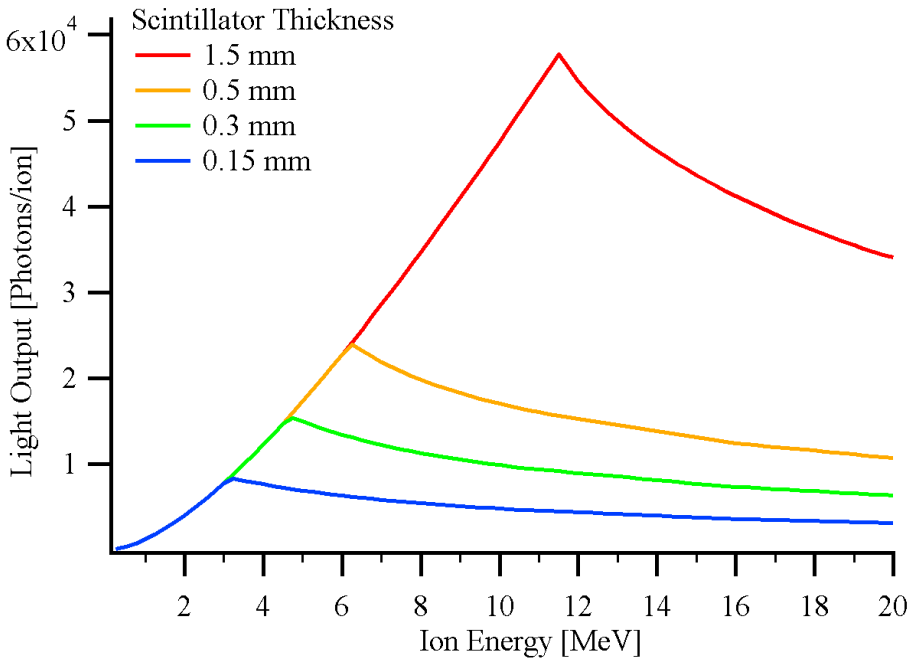

Figure 2.10: Spectral response function for protons in EJ-260 for different scintillator thicknesses

was included in their calibration using the equation

$$\frac{dL}{dx} = S\frac{\frac{dE}{dx}}{1 + k_B\frac{dE}{dx} + k_C\left(\frac{dE}{dx}\right)^2} \tag{2.15}$$

There are examples of this method being used to obtain a relative light yield on a similar PVT based plastic scintillator, EJ-228 [40]. Though there are no absolute calibrations of the response of these plastic scintillators, and no relative light yield measurements for EJ-260. Because of this, the quenching factors provided by Awe et al. act as a good first order estimation of the proton yield. A response function can be obtained using Equation 2.15, and the energy loss vs position in the scintillator similar to that seen in Figure 2.5. The proton stopping power data for PVT was estimated using SRIM [41], a software which uses a quantum mechanical treatment of ion-atom collisions to simulate the ion's path through matter. Similar to how the proton cutoff energy was calculated in the instrument calibration, the energy loss as a function of distance was used to compute the light yield as a function of distance. The results were integrated to get the total light yield for a single proton of a specific energy. The resulting spectral response function for protons

is seen Figure 2.10. There is a noticeable discontinuity in the response. This can be attributed to protons that transmit through the scintillator without encountering the Bragg peak energy loss. This means higher energy protons will transmit through the scintillator without depositing a significant fraction of their energy.

A Python script was written to automatically scan for new images as they are saved from a shot, and retrieve the spectrum. A few inputs were required such as the position of the x-ray/neutral zero order, the scale of the image in question (pixels to cm), and the ion species of interest. Though these would remain constant throughout a shot series and would not interfere with HRR operation. The deflection of the ion species of interest was estimated using a polynomial fit to the deflection traces from the simulation code seen in Figure 2.4. The position of the parabolic trace for the species of interest with respect to the zero-order was estimated by the deflection results from the simulation in Figure 2.4. A background subtraction is performed by sampling the noise along the magnetic deflection line where no trace bisects and removing x-ray hard hits with a median filter. Dispersion binning is the integration of signal over a range of ion energies due to the finite pixel size of the camera. The value was different along the magnetic deflection due to the non-linear sweep of ion energies. Once calculated this was accounted for in the spectrum. Lastly, the code deconvolves the spectral response function, seen in Figure 2.10, from the raw data trace in order to retrieve the estimated proton yield per unit steradian. In addition, the ion characteristic temperature and cutoff energy were measured. A sample of the resulting spectrum can bee seen in Figure 2.11 This code provides a mechanism to achieve on-shot spectral analysis. As will be discussed later, this is a necessity for single-shot closed-loop neural network training for LIA optimization.

2.3.2 High Repetition Rate Experimental Results and Analysis

For demonstration purposes, a high repetition rate experiment was performed in a different configuration than the calibration setup. One of the main limitations of the f/2 beamline is the laser's short Rayleigh range of approximately 20 μm. This means that any small variation in flatness in the target holder or of the target foil itself could result in defocusing of the target. As

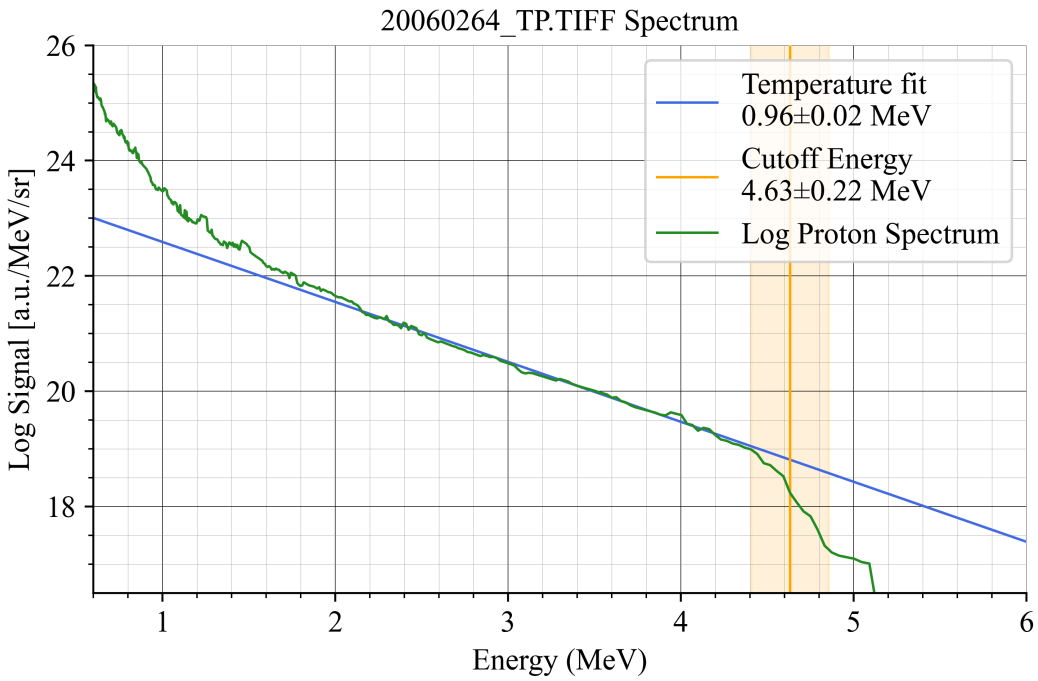

Figure 2.11: Sample of proton spectrum showing automatic temperature fit and cutoff energy calculation

a result, each target in the f/2 configuration must be manually aligned to the focus of the laser using a front surface imaging system. This creates a maximum firing rate of approximately one shot per minute. One way to circumvent these issues is to use the f/25 beamline available at CSU. The 4.7 m focal length provides conveniently long Rayleigh range of approximately 2 mm at the fundamental frequency, which relaxes the requirements on targeting positioning accuracy. This allows us to perform an initial alignment of a target and safely assume the subsequent target positions to be in focus for the rest of the series. Through the use of motorized target motion in conjunction with an automated G-code controlled positioning system we were able to reliably and rapidly position each target in the holder, achieving a shot rate of 0.2 Hz on solid targets.

The first demonstration of data collection at high repetition rate consisted of a scan of the lase intensity. The laser energy was varied from 3 J to a maximum of 21 J. The resulting cutoff energies are seen in Figure 2.13. For comparison, the predicted cutoff energy based on the Fuchs model according to Equation 1.17 is plotted. The model results were obtained using the hot electron temperature scaling given by Wilkes in Equation 1.16, a pulse duration of 45 fs, a target thickness of

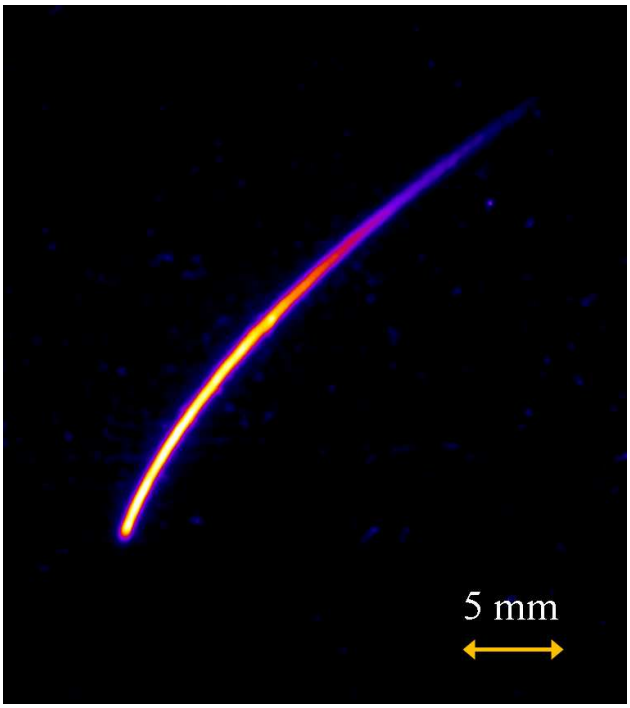

Figure 2.12: Example of proton trace in a high repetition rate run

9 μm, a spot size of 50 μm. We see a significant deviation between the measured results and those predicted by the model which appears to drastically under-predict the experimental cutoff energy. Brenner et al. [42] proposed a modification of the Fuchs model by modifying the acceleration time. Fuchs fixed the acceleration time to the laser pulse length by $\tau_{acc} = 1.3t_{laser}$. Though this isn't physically accurate, it agreed well with simulations. Brenner proposed the inclusion of two additional terms beyond the laser pulse duration accounting for the acceleration time of the ions. The first, $\tau_{expansion}$, is the time it takes for the ions to expand beyond the sheath region and thus for the transfer of energy from the electrons to protons to dissipate. Buffechoux et al. [43] gives a simple relation for the expansion time as $\tau_{expansion} = \frac{6}{\omega_{pi}}$. Additionally Brenner introduces a term, τ_{escape}, which accounts for time it take for axial electrons to escape lateral extent of the sheath. We can write this escape time as $\tau_{escape} = \frac{D_l}{2u_e}$. Here D_{Laser} is the focal spot diameter and u_e is the average velocity of the electrons driving the acceleration process which can be taken from the electron distribution function in Equation 1.15. The new acceleration time will be the magnitude

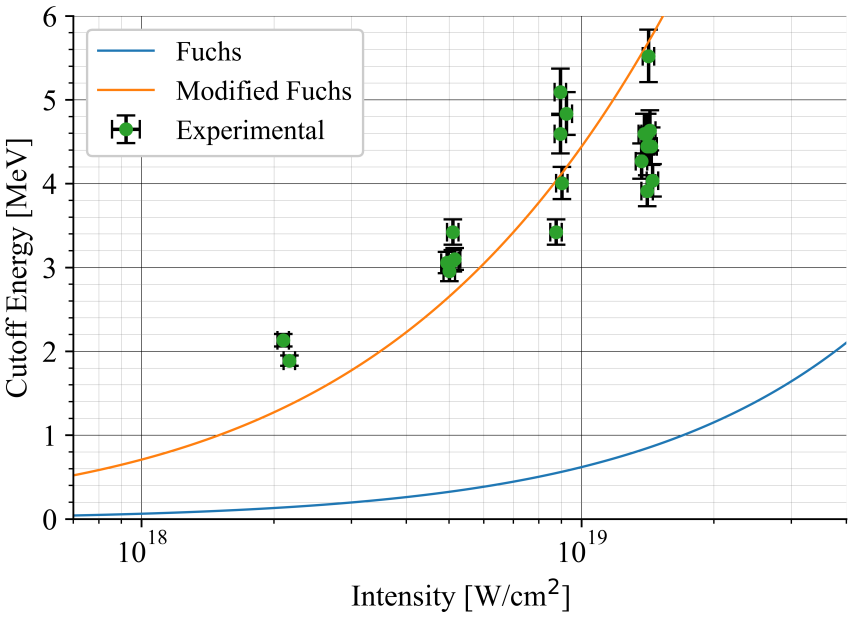

Figure 2.13: Intensity scan of proton cutoff energy by varying incident laser energy. The expected Fuchs relation between laser intensity and cutoff energy is plotted along with a modified Fuchs model.

of these 3 terms and is given as

$$\tau_{acc} = \sqrt{\tau_{Laser}^2 + \tau_{expansion}^2 + \tau_{escape}^2} \tag{2.16}$$

The modified-Fuchs scaling for the laser parameters at ALEPH are plotted against the results in Figure 2.13. We can see this fits better with the experimental results compared to the basic Fuchs model. Much of the difference can be attributed to in part the large focal spot size increasing the lateral escape time.

We can see that laser and plasma parameters strongly effect the max energy scaling of laser accelerated protons. However, finding the best conditions for LIA can be a daunting task due to the sheer number of input parameters at play. Intensity, scale length, pulse duration, contrast, target thickness, electron density, among many others have drastic effect on the heating, transport, and acceleration mechanisms involved. Scanning the parameter space necessary to optimise this interaction is nearly impossible with the more conventional particle-in-cell (PIC) simulation analysis typically encountered in the field [44, 45]. Therefore a main direction of the development of

an HRR TP is the implementation of HRR diagnostics in conjunction with a neural network (NN) trained to predict laser pulse shapes to optimize the laser matter interaction, in our case for LIA. We are developing this approach in collaboration with a group at Lawrence Livermore National Lab [46]. A first implementation of this artificial intelligence based laser pulse shape optimization was performed via a parameter scan of the acousto-optic modulator at the front end of the laser. The NN had been trained previously and output a list of predictive pulse shape parameters. We note that the scans performed so far were done without feedback from the run. We can conclude that this is a mode of operation that is now possible with HRR data collection an analysis of the type presented in this thesis. The combination of the HRR trace capture and the suite of on-shot spectrum retrieval and analysis software will enable us to operate in conjunction with a neural network training program to uncover the conditions best suited to MeV ion acceleration. Future experiments are planned where we would have live feeding of the results from a shot to re-train the NN and have it predict a new set of optimized conditions. This closed loop NN training and laser parameter prediction would be the first laser solid-matter interaction experiment controlled by artificial intelligence.

2.4 Outstanding Issues

Though much of the rep-rated instrument operation showed promising results, there were unresolved issues that put limitations on HRR runs at the highest laser intensities. For the results obtained above, the laser energy was limited to $11 - 12$ J, short of the maximum capability of the system of 25 J on target. At the low energy operation conditions, the instrument was well-behaved. We were able to obtain clean spectra from nearly every shot taken in the series. However, for the cases where the laser energy was increased up to its maximum capabilities for energy on target, some abnormalities in the ion traces began to appear and become more frequent. Two of the main phenomena observed were EMP related trace distortions and low energy trace blooming due to pinhole charging. Short pulse laser facilities have a propensity to excite powerful bursts of EMP [47]. As electrons and other charged particle are accelerated in the plasma source, they

(a) **(b)**

Figure 2.14: Examples of trace abnormalities where a) is due to EMP related trace distortions and b) is due to pinhole charging

propagate throughout the interaction chamber and collide with the walls and other components. This impulse of charged particle collisions results in a broad-spectrum RF electromagnetic wave emission. This EMP is able to interact with sensitive electronics, often damaging cameras or tripping the HV power supplies for the Thomson parabola. This EMP also has the ability to affect the operation of the instrument itself where the RF excitation can affect the voltage of the electrodes and thus the electric field that the ions see as they deflect through the spectrometer [48]. This results in characteristic trace distortions which can bee seen in Figure2.14a. While these distortions ideally do not effect the spectral calibration of the instrument since the instrument parameter variation is in the electrode voltage, and thus not the magnetic deflection, the distortions may disrupt the ability of our software to retrieve an on-shot spectrum and may cause different charge states of ions to overlap, making resolving a spectrum potentially impossible. Methods to mitigate this effect were discussed by Morrison et al. [29]. This included the addition of a low pass filter to the HV cabling to reduce the influence of the RF interference. An additional solution includes proper shielding of the instrument in a carefully designed Faraday cage.

Another trace distortion mechanism seen at higher laser energies was pinhole charging. As described before energetic electrons emitted from the plasma source are able to collide with different components in the interaction chamber. If enough of these electrons collide with the brass pinhole of the spectrometer, the metal will begin to build up a net negative charge effectively creating an Einzel lens. As ion propagate through the pinhole they will begin to lens where the low energy region of the ion trace blooms significantly. This effect can be seen in Figure 2.14b. We can note that the trace seen was obtained with the larger 680 μm pinhole compared to the more frequently used 300 μm pinhole. Therefore the unperturbed ion trace is thicker than normal. Similar to the EMP related trace distortions, pinhole charging may cause enough blooming of the traces, especially at lower energies, such that different ion charge states may begin to overlap. Making resolving a spectrum impossible. Additionally, blooming may cause the spectral resolution of the instrument to decrease significantly enough that the results lack significance. One measure taken to reduce this trace distortion was ensuring the body of the TP had good electrical contact with the ground. Since the instrument sits on an anodized 3-axis rotation stage this had acted as a form of electrical insulation between the body of the TP and the interaction chamber which is grounded. The simple addition of a copper wire attached from the chamber floor to the instrument near the pinhole has acted to reduce the occurrence of pinhole charging.

Chapter 3

Novel Scheme For the Generation of Spike Trains of Uneven Delay and Duration

3.1 Laser Plasma Instability and Control

One of the most exciting areas of research today is the study of schemes for fusion energy, and the hope that it may provide access to unlimited clean energy. There are two competing fusion energy schemes - Inertial Confinement Fusion (ICF) and Magnetic Confinement Fusion (MCF). One of the oldest attempts at the generation of fusion energy was the z-pinch wherein a plasma column is pulsed with extremely high current. The resulting magnetic field creates a cylindrical compression on the plasma column which would hopefully compress enough to create the plasma conditions for fusion energy generation [49–51]. Tokamaks [52–54] and Stellerators [55, 56] are currently the most promising tools for magnetic confinement fusion energy, wherein hydrogen plasma is confined by a network of superconducting electromagnets or permanents magnets respectively.

A different approach to fusion energy is based on ablative compression of a fuel pellet. These systems use some of the most powerful and energetic lasers in the world to compress a small fuel pellet to extreme temperatures and densities sufficient to drive a fusion reaction. The leading example of this technology is the National Ignition Facility (NIF). This laser system consists of 192 of Nd:glass amplified 1.052 μm beams that are frequency tripled to 351 nm delivering 1.8 MJ of laser light on target with peak powers of 500 TW [57]. For the so-called indirect drive configuration, the $3\omega_0$ light enters into a capsule known as a hohlraum, depicted in Figure 3.1. This capsule acts as both a housing for the fuel and as a conversion mechanism for the $3\omega_0$ light. As it impinges on the inner walls coated with gold (Au) or depleted uranium (DU), the light is converted to soft (keV) x-rays with efficiencies exceeding 80% [58]. From here the x-rays bathe the fuel pellet sus-

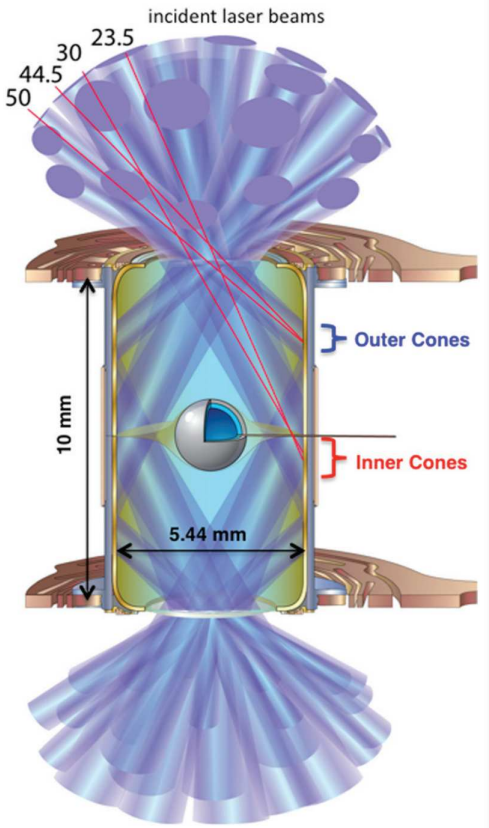

Figure 3.1: Hohlraum image from reference [2]

pended in the center of the hohlraum. This pellet consists of an external 2 mm diameter ablative layer typically consisting of copper/beryllium or CH, a 75 μm cryogenic deuterium-tritium (DT) ice layer with submicron variation, and an inner gaseous DT core [59]. As the x-rays bathe the outer shell, material ablates outward and through conservation of momentum drives the rest of the pellet inward which can be described by a spherical rocket equation [60]. This creates a central hot spot where the fusion reaction begins and creates a self-sustaining outward propagating burn [61]. This compression is extremely sensitive to hydrodynamic instabilities [62]. Additional instabilities put limits on the x-ray flux variation to $< 8\%$ rms on the pellet itself [63–65]. This requirement is made difficult due to various absorptive parametric instabilities that can occur as the laser light propagates through the hohlraum to the Au/DU walls.

Two of the main absorptive parametric instabilities seen in these driven fusion plasmas are Stimulated Brillouin Scattering (SBS) and Stimulated Raman Scattering (SRS). SBS can be de-

scribed as the coupling and decay of a laser photon into a scattered photon and an ion acoustic wave (IAW). SRS is a similar instability only it involves coupling of the laser photon into a scattered photon and an electron plasma wave EPW. As the laser light propagates in the hohlraum, it encounters the low density plasma region of the capsule. It can resonantly excite these parametric instabilities where it creates an internal "mode"(the wave) and back-scattered light. This back-scattered light and the incident light can parametrically excite new plasma waves, creating an unstable positive feedback loop where these scatter processes grow exponentially. This leads to a decrease in efficiency of the conversion of laser light to x-rays. Additionally, it results in scatter light directly impinging on the pellet, creating hot spots, and thus seeding hydrodynamic instabilities.

The SRS interaction can be described by momentum and energy conservation in the dispersion relation

$$\begin{aligned} \omega_0 &= \omega_s + \omega_{EPW} \\ k_0 &= k_s + k_{EPW} \end{aligned} \tag{3.1}$$

The minimum frequency the wave can propagate in the plasma is $\omega_0 = \omega_{pe}$. This limits the SRS instability to $\omega_0 \geq 2\omega_{pe}$ or $n_e \leq \frac{n_c}{4}$. The Raman gain can be written as [60]

$$G_{SRS} = \frac{1}{8} \frac{k_l^2 v_0^2}{\omega_0 \omega_r} \frac{\omega_l}{v_l} \frac{\omega_0}{v_{gr}} L \tag{3.2}$$

where v_0 is the quiver velocity of an electron in the laser field, ω_r is the scattered Raman wave frequency, ω_l is the EPW frequency, v_l is the EPW damping rate, v_{gr} is the group velocity of the EPW and L is the length over which the three-wave resonance occurs. The threshold intensity for SRS gain is $I^{SRS} \geq \frac{40}{L_N \lambda_0}$ where L_N is the density scale length for the $\frac{n_c}{4}$ density in μm, and λ_0 is

the center wavelength in μm [66]. Similarly for SBS

$$\begin{aligned} \omega_0 &= \omega_s + \omega_{IAW} \\ k_0 &= k_s + k_{IAW} \end{aligned} \tag{3.3}$$

Since ω_{IAW} is much smaller than the frequency of the laser, the SBS instability can occur throughout the underdense plasma region.

$$G_{SBS} = \frac{1}{8}\frac{v_0^2}{v_e^2}\frac{n_e}{n_c}\frac{\omega_a}{v_a}\frac{\omega_0}{v_{gb}}L \tag{3.4}$$

where, v_0 and v_e are the electron quiver velocity and thermal velocity, ω_a is the IAW frequency, v_a is the IAW damping rate, v_gb is the group velocity of the IAW. The threshold intensity for which this instability occurs in the underdense region is given by $I^{SBS} \geq 1.7\frac{T_e}{(n/n_C)\lambda_0 L_u}$, where T_e is the electron temperature and L_u is the velocity scale length [66]. The exponential gain that these parametric instabilities experience leads to detrimental effects in the operation of an ICF system.

One proposed solution is to deposit the laser energy by the use of a spike train of uneven delay and duration (STUD pulses) [67, 68]. These pulse trains drive the implosion process in a similar manner to a normal ICF configuration. However, the pulse is broken into this pulse train which excites the same parametric instabilities, only now the LPIs are not allowed to grow exponentially through the entire pulse duration. The light is essentially turned off during the off-duty cycle, allowing the IAW and EPW to damp in between excitations. Once the next pulse in the train comes on, there is less of a seed of the instability to grow. This has been shown in simulations to lead to drastic reductions in the SRS and SBS instabilities as seen in the normal configuration. Because of this, this technique shows promise as better driver of the implosion process. Here we present a simple scheme for the generation of these STUD pulses. In the typical setup at the ALEPH laser facility's f/25 beamline, several planar turning mirrors are used in the laser chain to route the 185 mm diameter beam after pulse compression to the f/25 off axis parabola, where it focuses over 4.7 m down to a near diffraction limited spot size of approximately 50 μm in diameter.

Our scheme for generating STUD pulses revolves around replacing one of these planar mirrors in the laser chain with a custom-made hexagonal step mirror shown in Fig.3.2.

3.2 Step Mirror Design

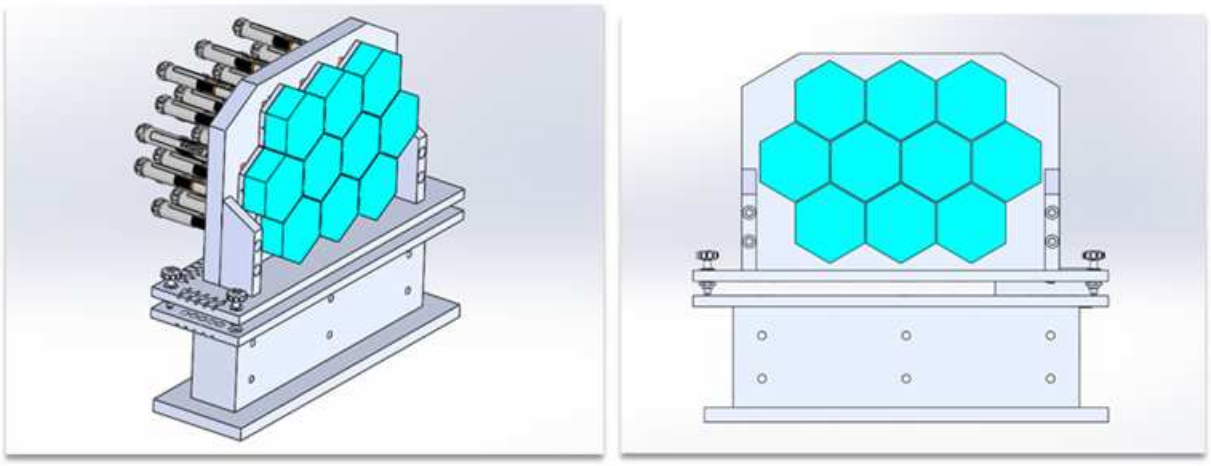

Figure 3.2: Diagram of STUD-forming mirror based on adaptive optics

The STUD-forming step mirror consists of 10 hexagonal mirrors actuated by an array of motors an mounted on a common body/frame. Each mirror segment is held in position and controlled by 3 Thorlabs Z812V motorized actuators. These actuators give us tip and tilt control of each of the mirror segments. Additionally, all three motors can be translated in or out to achieve "piston" control of the beamlets. The main goal of this segmented mirror is to spatially offset the plane at which the laser wavefront reflects from. When the plane of one mirror segment is offset from the plane of another mirror segment, the optical path length (OPL) of the wavefront at one mirror face will be different than the OPL of the wavefront reflecting off another mirror segment creating a time delay between the pulses. This wavefront division scheme, illustrated in Figure 3.3, generates 10 individual sub-pulses from each of mirror segments which can be temporally offset from one another. As the these individual beamlets propagate further through the laser chain and through the OAP, they will focus down to the same spot, however they will arrive at different times according to

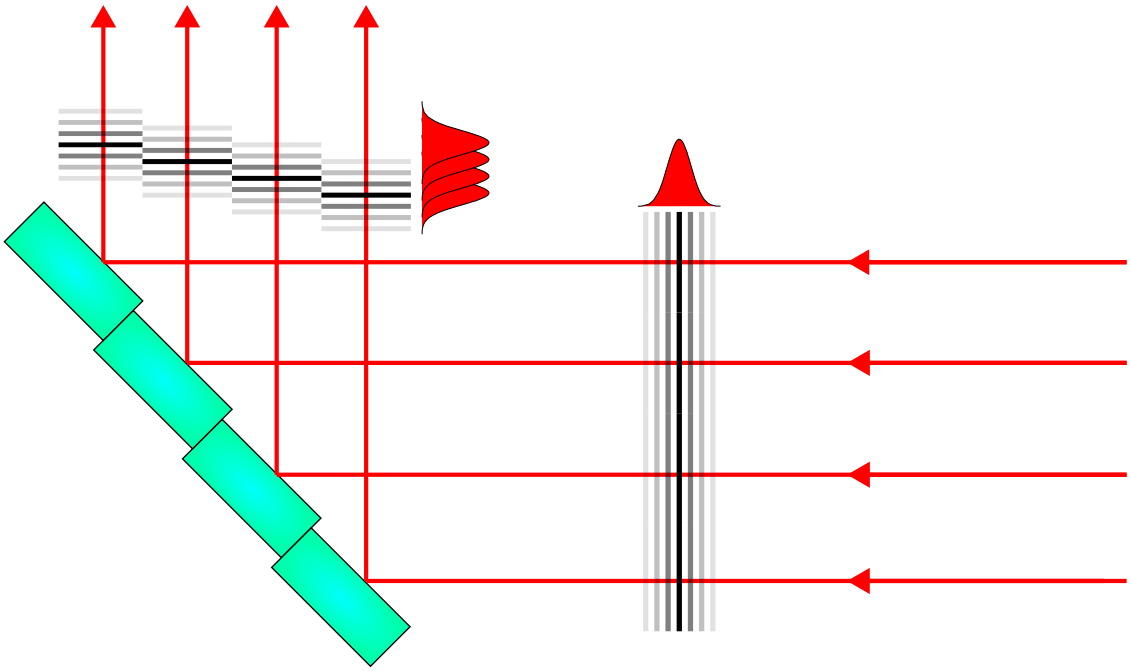

Figure 3.3: Illustration of STUD mirror operation. The initially flat wavefront is divided due to the segmented mirrors, The offset of each mirror creates a delay between the divided wavefronts.

the optical path difference. This effectively creates a pulse train, with arbitrary separation between each sub-pulse, at the laser focus.

3.2.1 Pulse Timing and Alignment

The timing of the pulses began by choosing a mirror segment to act as the reference time/optical path length. The procedure consists of overlapping the focal spot of two beamlets at a time, and changing the pulse duration until they are close enough temporally so that they interfere. This means that the pulses are within a time Δt that is less than the coherence time defined as:

$$\tau_{coh} = \frac{\lambda_0^2}{c\Delta\lambda} \tag{3.5}$$

where λ_0 is the laser center wavelength and $\Delta\lambda$ is the bandwidth of the pulse. For the laser's typical operating bandwidth of $\Delta\lambda \approx 20$ nm, the coherence time is $\tau = 106$ fs and the coherence length is $l_{coh} = 32$ μm. The short distance over which each of the beamlets interfere makes the task of temporally overlapping all the pulses using this technique challenging. To mitigate this and

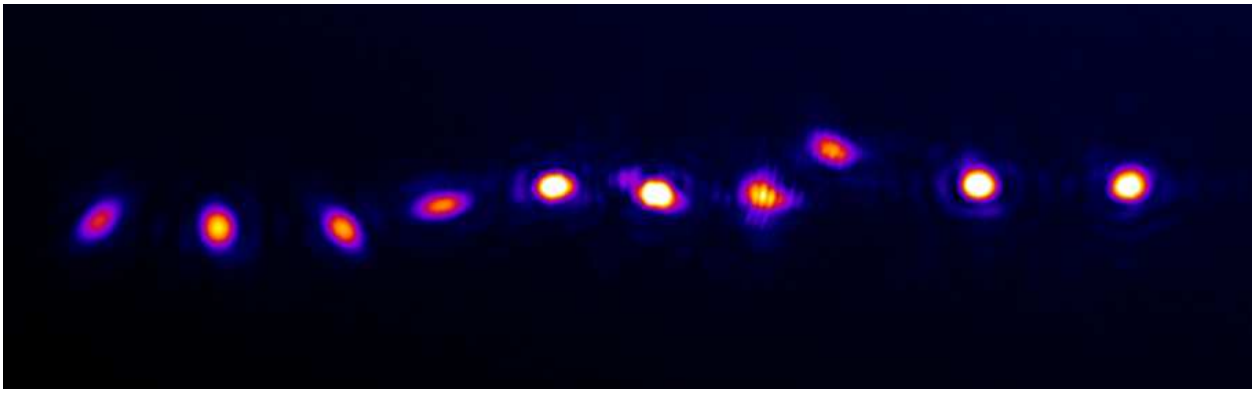

(a)

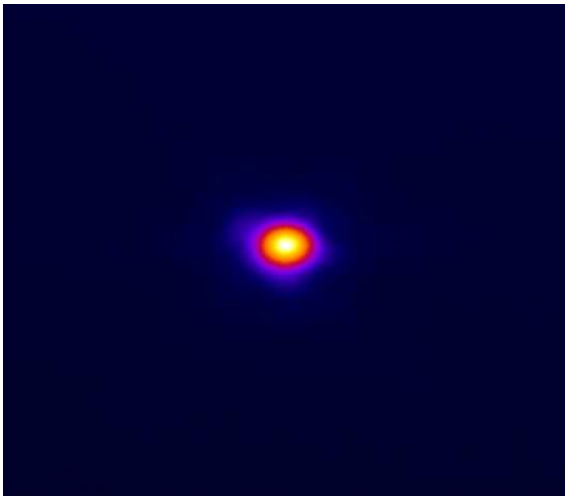

(b)

Figure 3.4: Resulting focus of STUD-forming mirror array where a) shows the spot foci of 10 individual beamlets timed to t_0 with visible fringing and b) shows the resulting spot focus from the overlap of the 10 beamlets with 200 fs pulse separation

ease the task of timing the pulses, we used the Dazzler, an acousto-optic modulator on the front end of the laser to cut the band width of the laser. To start the procedure, We cut the bandwidth to 1 nm. This extends the coherence length of the laser pulses to 0.64 mm. Once fringes appear, the bandwidth is increased to 5nm and the path length is adjusted again to bring the pulses to within the coherence time. This is repeated at $10/$;nm and so on, until fringes are visible with the full bandwidth. This meant the sub-pulses are timed to within 106 fs and the mirror surfaces are flat with each other to within 23 μm. This is different from the coherence length due to a factor of $\sqrt{2}$ arising due to the 45° angle between the mirrors and laser wavefront. This procedure is repeated for each of the 10 mirrors in the STUD-forming array. To improve the resolution of our t_0 timing

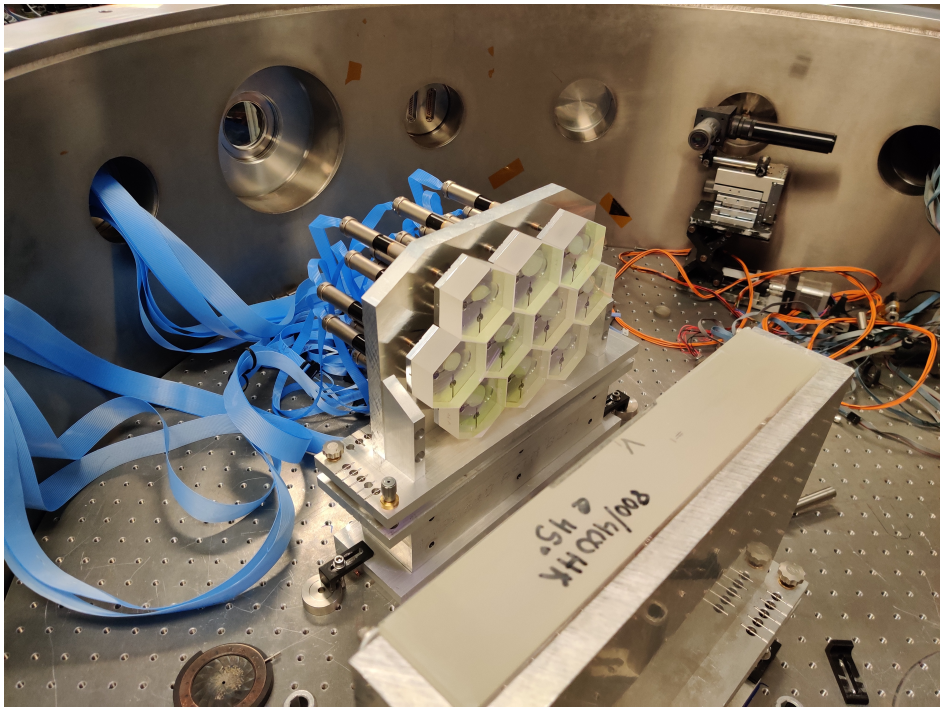

Figure 3.5: STUD Mirror in Experimental Configuration

even further, we step through the coherence length for the mirror in steps of 1 μm, from where the interference pattern appears to where the fringes disappear again. Subsequently, we split the difference and move to the center of the coherence length amounting to a spatial resolution of 1 μm and a temporal resolution of ± 4.7 fs. The results from this t_0 timing are shown in Figure 3.4a. From this point forward any of the timing done for the sub-pulses is done by tracking the relative positions of the mirrors from their t_0 position. Once offset temporally, the beamlets are overlapped spatially. The result of stacking the 10 pulses is shown in Figure 3.4b. We can see the smooth image of the stacked foci. This image was taken for a pulse separation of 200 fs which is greater than the coherence length of the pulses, thus there was no fringe formation. Characterization of the full pulse train is still needed where a cross-correlation measurement would suffice.

3.3 Experimental Results

A commissioning experiment wuth the STUD-forming mirror was performed at the ALEPH laser system. We explored the STUD pulse parameters best suited to LPI control and mitigation in

a resonance absorption experiment. Recall the discussion earlier of the electron heating mechanism by which laser light is refracted through the plasma to a electron density given by $n_e = n_c \cos^2(\theta_i)$. The evanescent wave tunnels to the critical density, where it resonantly drives EPW's at ω_L. The laser light can couple to the EPW's generated at the critical density to emit $2\omega_0$ light [69–71]. We can contrast this with the SRS back-scattered light that we would observe from the instability scattering. The SRS scattered light will emit according to the given dispersion relation in Equation 3.1. At $\frac{n_c}{4}$, we get $\omega_0 = 2\omega_{EPW}$. The SRS light will correspond to side-lobes around the laser frequency at both $\frac{3\omega_0}{2}$ and $\frac{\omega_0}{2}$ with each sidelobe extending toward the central frequency for plasma densities below $\frac{n_c}{4}$, though the strongest emission will be at resonance. We can use this characteristic emission for light that couples to the critical density as an indication of absorption to the plasma. Similarly, the emission at these SRS side-lobes will act as characteristic indications of light that scatters at quarter critical or below.

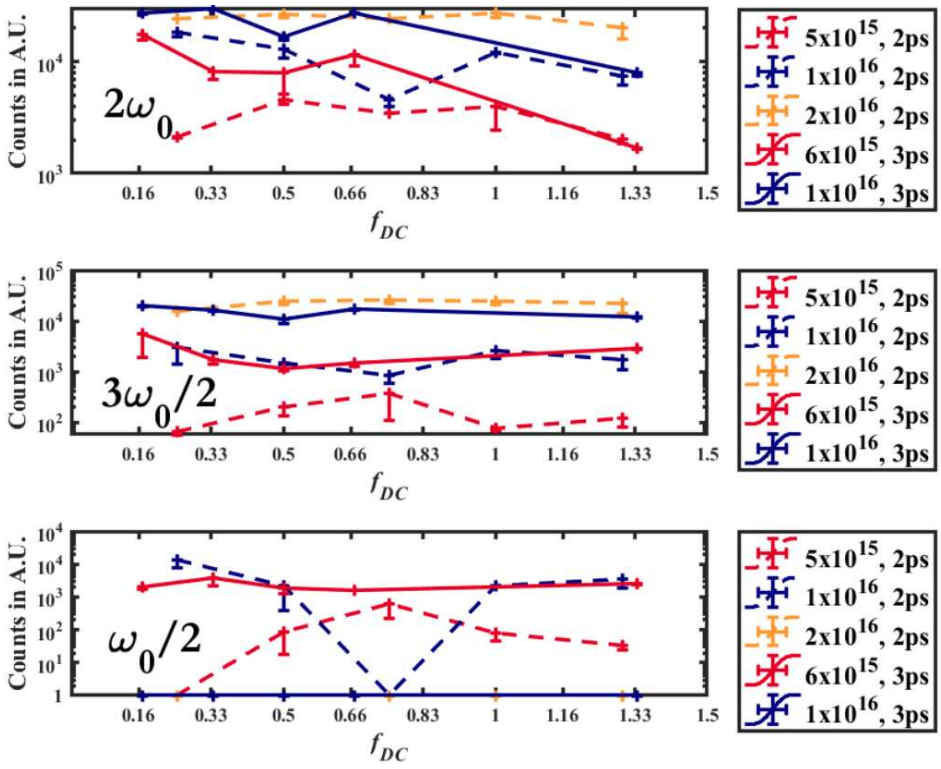

Figure 3.6: Sample of experimental results for the investigation of STUD pulse based mitigation of SRS laser plasma instabilities. $2\omega_0$, $3\omega_0/2$, and $\omega_0/2$ emission from 2 and 3 ps pulses for various duty cycles.

The experiment was performed in the ALEPH laser system's f/25 interaction chamber/beamline. A pre-plasma was generated by an uncompressed 320 fs, 800 nm heater beam focused by a 5 m lens to a 140 μm spot incident near normal on the target surface. The STUD beam was transported along the typical f/25 beamline, obliquely incident on the target surface. Optical fiber spectrometers were placed in the back scatter direction and in the specular direction. The $2\omega_0$, $\frac{3\omega_0}{2}$, and $\frac{\omega_0}{2}$ were observed in the back-scatter direction with the $2\omega_0$ and $\frac{3\omega_0}{2}$ seen with one spectrometer and the $\frac{\omega_0}{2}$ seen on a dedicated long wavelength spectrometer. Specularly reflected 800 nm light was monitored by a fiber spectrometer to observe any incident laser light not coupled to the plasma. A wide parameter space was explored where we varied the delay between STUD pulse, individual pulse separation, pulse duration, STUD beam intensity, angle between the STUD pulse and the target, and heater pulse energy. We first set out to optimize the resonance absorption conditions for the best $2\omega_0$ signal. In this optimization the planar mirror in the f/25 beamline was not replaced with the STUD mirror, so we worked with 2 ps single pulses. The first optimization began by tuning the angle between the f/25 beam and the target from 10° to 40° settling on 20°. Additionally, we tuned the plasma scale length for optimized RA by varying the heater delay between -100 fs and $+500$ fs, settling on $+200$ fs. The effect of the STUD pulses on the SRS instability was then explored with the STUD mirror being placed in the beamline. We varied the energy of the pulses, with the intensity ranging from 10^{14} to 10^{17} W/cm^2. Lastly, the individual pulse separation and duty cycle were varied for 2 and 3 ps global pulse durations. In all, we collected > 5000 shots with strong shot to shot variation. A summary of results from some of these shots for differing duty cycles are shown in Figure 3.6. A cursory examination of the data indicates increased $2\omega_0$ emission for 50 fs STUD pulse duration compared to 260 fs implying more laser light coupling to the critical density for lower duty cycles compared to a single long pulse beam. Though preliminary results indicate the ability of STUD pulses to reduce the SRS instability and increase coupling of laser light to the critical density, there are currently 1000's of shots that are in the process of being analyzed.

Chapter 4

Summary

We have designed, built, calibrated, and tested a compact Thomson parabola ion spectrometer capable of operating at 10's of Hz. Additionally, a suite of ion spectrogram retrieval and analysis software was developed to aid the operation and data collection capabilities of the system. We have demonstrated this diagnostic is capable of operating without the use of an intensifying screen or MCP which both simplifies the diagnostic operation and makes it more robust to the harsh EMP environments of high-intensity short-pulse driven experiments. The rapid data collection, enabled by the combination of this instrument with high repetition rate lasers, will allow for large multivariate parameters scans to better diagnose complex plasma conditions, allow for studies on sources of ion beam variation, and enable experiments driven by artificial intelligence algorithms [72]. Commissioning experiments in conjunction with neural network optimization of laser parameters was performed. Future work would involve live training and feedback from the neural network algorithms to aid the optimization of laser and plasma conditions for MeV ion acceleration.

In addition, we designed, built, and implemented a novel STUD pulse generation mechanism using an adaptive array of hexagonal mirrors. This STUD pulse generation method offers a simple and robust method of generating a pulse train of arbitrary delay in high intensity laser systems for the study laser plasma instability mitigation. Taking inspiration from the work performed on the Thomson parabola, future work may involve the implementation of rep-rated diagnostic and machine learning algorithms to study the STUD pulse configuration best suited to mitigating laser plasma instabilities and increasing the efficiency and stability of ICF mechanisms.

Bibliography

[1] J. B. Birks. *The theory and practice of scintillation counting / by J.B. Birks*. Pergamon Press Oxford [England], 1964.

[2] D. E. Hinkel, M. D. Rosen, E. A. Williams, A. B. Langdon, C. H. Still, D. A. Callahan, J. D. Moody, P. A. Michel, R. P. J. Town, R. A. London, and S. H. Langer. Stimulated raman scatter analyses of experiments conducted at the national ignition facility. *Physics of Plasmas*, 18(5):056312, 2011.

[3] Donna Strickland and Gerard Mourou. Compression of amplified chirped optical pulses. *Optics Communications*, 56(3):219–221, 1985.

[4] Colin N. Danson, Constantin Haefner, Jake Bromage, Thomas Butcher, Jean-Christophe F. Chanteloup, Enam A. Chowdhury, Almantas Galvanauskas, Leonida A. Gizzi, Joachim Hein, David I. Hillier, and et al. Petawatt and exawatt class lasers worldwide. *High Power Laser Science and Engineering*, 7:e54, 2019.

[5] Paul Gibbon. *Short Pulse Laser Interactions with Matter*. PUBLISHED BY IMPERIAL COLLEGE PRESS AND DISTRIBUTED BY WORLD SCIENTIFIC PUBLISHING CO., 2005.

[6] Hong-bo Cai, Wei Yu, Shao-ping Zhu, Chun-yang Zheng, Li-hua Cao, and Wen-bing Pei. Vacuum heating in the interaction of ultrashort, relativistically strong laser pulses with solid targets. *Physics of Plasmas*, 13(6):063108, 2006.

[7] Hong-bo Cai, Wei Yu, Shao-ping Zhu, and Chun-yang Zheng. Short-pulse laser absorption via j×b heating in ultrahigh intensity laser plasma interaction. *Physics of Plasmas*, 13(11):113105, 2006.

[8] S. Pfalzner. *An Introduction to Inertial Confinement Fusion*. Series in Plasma Physics. CRC Press, 2006.

[9] S. C. Wilks, W. L. Kruer, M. Tabak, and A. B. Langdon. Absorption of ultra-intense laser pulses. *Phys. Rev. Lett.*, 69:1383–1386, Aug 1992.

[10] M. G. Haines, M. S. Wei, F. N. Beg, and R. B. Stephens. Hot-electron temperature and laser-light absorption in fast ignition. *Phys. Rev. Lett.*, 102:045008, Jan 2009.

[11] A. Pukhov, Z.-M. Sheng, and J. Meyer-ter Vehn. Particle acceleration in relativistic laser channels. *Physics of Plasmas*, 6(7):2847–2854, 1999.

[12] Marius Schollmeier. *Optimization and control of laser-accelerated proton beams*. PhD thesis, 01 2008.

[13] R. A. Snavely, M. H. Key, S. P. Hatchett, T. E. Cowan, M. Roth, T. W. Phillips, M. A. Stoyer, E. A. Henry, T. C. Sangster, M. S. Singh, S. C. Wilks, A. MacKinnon, A. Offenberger, D. M. Pennington, K. Yasuike, A. B. Langdon, B. F. Lasinski, J. Johnson, M. D. Perry, and E. M. Campbell. Intense high-energy proton beams from petawatt-laser irradiation of solids. *Phys. Rev. Lett.*, 85:2945–2948, 2000.

[14] Adam Higginson, Ross Gray, Martin King, Rachel Dance, Samuel Williamson, Nicholas Butler, Robbie Wilson, Rémi Capdessus, Chris Armstrong, Steve Hawkes, Philip Martin, Wenqing Wei, S. Mirfayzi, Xiaohui Yuan, Satya Kar, Marco Borghesi, Rob Clarke, David Neely, and Paul Mckenna. Near-100 mev protons via a laser-driven transparency-enhanced hybrid acceleration scheme. *Nature Communications*, 9:724, 02 2018.

[15] S. J. Gitomer, R. D. Jones, F. Begay, A. W. Ehler, J. F. Kephart, and R. Kristal. Fast ions and hot electrons in the laser–plasma interaction. *The Physics of Fluids*, 29(8):2679–2688, 1986.

[16] J. Fuchs, P. Antici, E. D'Humières, E. Lefebvre, M. Borghesi, E. Brambrink, C. A. Cecchetti, M. Kaluza, V. Malka, M. Manclossi, S. Meyroneinc, P. Mora, J. Schreiber, T. Toncian, H. Pépin, and P. Audebert. Laser-driven proton scaling laws and new paths towards energy increase. *Nature Physics*, 2(1):48–54, January 2006.

[17] P. Mora. Plasma expansion into a vacuum. *Phys. Rev. Lett.*, 90:185002, May 2003.

[18] Tatiana V. Liseykina, Marco Borghesi, Andrea Macchi, and Sara Tuveri. Radiation pressure acceleration by ultraintense laser pulses. *Plasma Physics and Controlled Fusion*, 50(12), Dec 2008.

[19] B. Qiao, M. Zepf, P. Gibbon, M. Borghesi, B. Dromey, S. Kar, J. Schreiber, and M. Geissler. Conditions for efficient and stable ion acceleration by moderate circularly polarized laser pulses at intensities of 1020 w/cm2. *Physics of Plasmas*, 18(4):043102, 2011.

[20] T Esirkepov, R Bingham, S Bulanov, T Honda, K Nishihara, and F Pegoraro. Coulomb explosion of a cluster irradiated by a high intensity laser pulse. *Laser and Particle Beams*, 18(3):503–506, Sep 2000.

[21] L. Yin, B. J. Albright, K. J. Bowers, D. Jung, J. C. Fernández, and B. M. Hegelich. Three-dimensional dynamics of breakout afterburner ion acceleration using high-contrast short-pulse laser and nanoscale targets. *Physical Review Letters*, 107:045003, Jul 2011.

[22] J. Badziak. Laser-driven ion acceleration: methods, challenges and prospects. In *International Conferences on Research and Applications of Plasmas (PLASMA-2017)*, volume 959 of *Journal of Physics Conference Series*. Inst Plasma Phys & Laser Microfus, 2018.

[23] David J. Stark, Lin Yin, Brian J. Albright, William Nystrom, and Robert Bird. A detailed examination of laser-ion acceleration mechanisms in the relativistic transparency regime using tracers. *Physics of Plasmas*, 25(4):043114, 2018.

[24] Yong Wang, Shoujun Wang, Alex Rockwood, Bradley M. Luther, Reed Hollinger, Alden Curtis, Chase Calvi, Carmen S. Menoni, and Jorge J. Rocca. $0.85pw$ laser operation at $3.3hz$ and high-contrast ultrahigh-intensity $\lambda = 400nm$ second-harmonic beamline. *Opt. Lett.*, 42:3828–3831, Oct 2017.

[25] Tae-won Jeong, Prashant Singh, C Scullion, Hamad Ahmed, Prokopis Hadjisolomou, C Jeon, H Yun, K Kakolee, Marco Borghesi, and S Ter-Avetisyan. Cr-39 track detector for multi-mev ion spectroscopy. *Scientific Reports*, 7, 05 2017.

[26] D. Nikezic and K.N. Yu. Formation and growth of tracks in nuclear track materials. *Materials Science and Engineering: R: Reports*, 46(3):51–123, 2004.

[27] T. Bonnet, M. Comet, D. Denis-Petit, F. Gobet, F. Hannachi, M. Tarisien, M. Versteegen, and M. M. Aleonard. Response functions of fuji imaging plates to monoenergetic protons in the energy range 0.6–3.2 mev. *Review of Scientific Instruments*, 84(1):013508, 2013.

[28] Joseph John Thomson. bakerian lecture:—rays of positive electricity. *Proceedings of the Royal Society of London. Series A, Containing Papers of a Mathematical and Physical Character*, 89(607):1–20, 1913.

[29] J. T. Morrison, C. Willis, R. R. Freeman, and L. Van Woerkom. Design of and data reduction from compact thomson parabola spectrometers. *Rev. Sci. Instrum.*, 82(3):033506, 2011.

[30] D.C. Carroll, P. Brummitt, D. Neely, F. Lindau, O. Lundh, C.-G. Wahlström, and P. McKenna. A modified thomson parabola spectrometer for high resolution multi-mev ion measurements—application to laser-driven ion acceleration. *Nucl. Instrum. Methods Phys. Res., Sect. A*, 620(1):23–27, 2010.

[31] Sadaoki Kojima, Shunsuke Inoue, Thanh Hung Dinh, Noboru Hasegawa, Michiaki Mori, Hironao Sakaki, Yoichi Yamamoto, Teru Sasaki, Keiichiro Shiokawa, Kotaro Kondo, Takashi Yamanaka, Masaki Hashida, Shuji Sakabe, Masaharu Nishikino, and Kiminori Kondo. Compact thomson parabola spectrometer with variability of energy range and measurability of angular distribution for low-energy laser-driven accelerated ions. *Review of Scientific Instruments*, 91(5):053305, 2020.

[32] K. Harres, M. Schollmeier, E. Brambrink, P. Audebert, A. Blažević, K. Flippo, D. C. Gautier, M. Geißel, B. M. Hegelich, F. Nürnberg, J. Schreiber, H. Wahl, and M. Roth. Development

and calibration of a thomson parabola with microchannel plate for the detection of laser-accelerated mev ions. *Review of Scientific Instruments*, 79(9):093306, 2008.

[33] Guido Van Rossum and Fred L. Drake. *Python 3 Reference Manual*. CreateSpace, Scotts Valley, CA, 2009.

[34] Peter Sigmund. *Particle Penetration and Radiation Effects Volume 2*, volume 179. 01 2014.

[35] C. G. Freeman, G. Fiksel, C. Stoeckl, N. Sinenian, M. J. Canfield, G. B. Graeper, A. T. Lombardo, C. R. Stillman, S. J. Padalino, C. Mileham, T. C. Sangster, and J. A. Frenje. Calibration of a thomson parabola ion spectrometer and fujifilm imaging plate detectors for protons, deuterons, and alpha particles. *Review of Scientific Instruments*, 82(7):073301, 2011.

[36] Martin Berger, J Coursey, and M Zucker. Estar, pstar, and astar: Computer programs for calculating stopping-power and range tables for electrons, protons, and helium ions (version 1.21), 1999-01-01 1999.

[37] J B Birks. Scintillations from organic crystals: Specific fluorescence and relative response to different radiations. *Proceedings of the Physical Society. Section A*, 64(10):874–877, oct 1951.

[38] D.L. Smith, R.G. Polk, and T.G. Miller. Measurement of the response of several organic scintillators to electrons, protons and deuterons. *Nuclear Instruments and Methods*, 64(2):157–166, 1968.

[39] C. Awe, P. Barbeau, A. Haghighat, S. Hedges, T. Johnson, S. Li, J.M. Link, V. Mascolino, J. Runge, J. Steenis, T. Subedi, and K. Walkup. Measurement of proton quenching in a plastic scintillator detector. *J. Instrum.*, 16(02):P02035–P02035, feb 2021.

[40] R.A. Weldon, J.M. Mueller, P. Barbeau, and J. Mattingly. Measurement of ej-228 plastic scintillator proton light output using a coincident neutron scatter technique. *Nucl. Instrum. Methods Phys. Res., Sect. A*, 953:163192, 2020.

[41] James F. Ziegler, M. D. Ziegler, and J. P. Biersack. SRIM - The stopping and range of ions in matter (2010). *Nuclear Instruments and Methods in Physics Research B*, 268(11-12):1818–1823, June 2010.

[42] C M Brenner, P McKenna, and D Neely. Modelling the effect of laser focal spot size on sheath- accelerated protons in intense laser–foil interactions. *Plasma Physics and Controlled Fusion*, 56(8):084003, jul 2014.

[43] S. Buffechoux, J. Psikal, M. Nakatsutsumi, L. Romagnani, A. Andreev, K. Zeil, M. Amin, P. Antici, T. Burris-Mog, A. Compant-La-Fontaine, E. d'Humières, S. Fourmaux, S. Gaillard, F. Gobet, F. Hannachi, S. Kraft, A. Mancic, C. Plaisir, G. Sarri, M. Tarisien, T. Toncian, U. Schramm, M. Tampo, P. Audebert, O. Willi, T. E. Cowan, H. Pépin, V. Tikhonchuk, M. Borghesi, and J. Fuchs. Hot electrons transverse refluxing in ultraintense laser-solid interactions. *Phys. Rev. Lett.*, 105:015005, Jul 2010.

[44] Joseph R Smith, Chris Orban, John T Morrison, Kevin M George, Gregory K Ngirmang, Enam A Chowdhury, and W Mel Roquemore. Optimizing laser–plasma interactions for ion acceleration using particle-in-cell simulations and evolutionary algorithms. *New Journal of Physics*, 22(10):103067, oct 2020.

[45] Joseph R. Smith, Chris Orban, Nashad Rahman, Brendan McHugh, Ricky Oropeza, and Enam A. Chowdhury. A particle-in-cell code comparison for ion acceleration: Epoch, lsp, and warpx. *Physics of Plasmas*, 28(7):074505, 2021.

[46] B. Z. Djordjević, A. J. Kemp, J. Kim, R. A. Simpson, S. C. Wilks, T. Ma, and D. A. Mariscal. Modeling laser-driven ion acceleration with deep learning. *Physics of Plasmas*, 28(4):043105, 2021.

[47] C G Brown, A Throop, D Eder, and J Kimbrough. Electromagnetic pulses at short-pulse laser facilities. *Journal of Physics: Conference Series*, 112(3):032025, may 2008.

[48] Filip Grepl, Josef Krása, Andriy Velyhan, Massimo De Marco, Jan Dostál, Miroslav Pfeifer, and Daniele Margarone. Distortion of thomson parabolic-like proton patterns due to electromagnetic interference. *Applied Sciences*, 11(10), 2021.

[49] Willard H. Bennett. Magnetically self-focussing streams. *Phys. Rev.*, 45:890–897, Jun 1934.

[50] R.L. Hagenson, A.S. Tai, R.A. Krakowski, and R.W. Moses. The dense z-pinch (DZP) as a fusion power reactor: preliminary scaling calculations and systems energy balance. *Nuclear Fusion*, 21(11):1315–1361, nov 1981.

[51] C.W. Hartman, G. Carlson, M. Hoffman, R. Werner, and D.Y. Cheng. A conceptual fusion reactor based on the high-plasma-density z-pinch. *Nuclear Fusion*, 17(5):909–918, oct 1977.

[52] R. Aymar, V.A. Chuyanov, M. Huguet, Y. Shimomura, ITER Joint Central Team, and ITER Home Teams. Overview of ITER-FEAT - the future international burning plasma experiment. *Nuclear Fusion*, 41(10):1301–1310, oct 2001.

[53] J. D. Strachan, H. Adler, P. Alling, C. Ancher, H. Anderson, J. L. Anderson, D. Ashcroft, Cris W. Barnes, G. Barnes, S. Batha, M. G. Bell, R. Bell, M. Bitter, W. Blanchard, N. L. Bretz, R. Budny, C. E. Bush, R. Camp, M. Caorlin, S. Cauffman, Z. Chang, C. Z. Cheng, J. Collins, G. Coward, D. S. Darrow, J. DeLooper, H. Duong, L. Dudek, R. Durst, P. C. Efthimion, D. Ernst, R. Fisher, R. J. Fonck, E. Fredrickson, N. Fromm, G. Y. Fu, H. P. Furth, C. Gentile, N. Gorelenkov, B. Grek, L. R. Grisham, G. Hammett, G. R. Hanson, R. J. Hawryluk, W. Heidbrink, H. W. Herrmann, K. W. Hill, J. Hosea, H. Hsuan, A. Janos, D. L. Jassby, F. C. Jobes, D. W. Johnson, L. C. Johnson, J. Kamperschroer, H. Kugel, N. T. Lam, P. H. LaMarche, M. J. Loughlin, B. LeBlanc, M. Leonard, F. M. Levinton, J. Machuzak, D. K. Mansfield, A. Martin, E. Mazzucato, R. Majeski, E. Marmar, J. McChesney, B. McCormack, D. C. McCune, K. M. McGuire, G. McKee, D. M. Meade, S. S. Medley, D. R. Mikkelsen, D. Mueller, M. Murakami, A. Nagy, R. Nazikian, R. Newman, T. Nishitani, M. Norris, T. O'Connor, M. Oldaker, M. Osakabe, D. K. Owens, H. Park, W. Park, S. F.

Paul, G. Pearson, E. Perry, M. Petrov, C. K. Phillips, S. Pitcher, A. T. Ramsey, D. A. Rasmussen, M. H. Redi, D. Roberts, J. Rogers, R. Rossmassler, A. L. Roquemore, E. Ruskov, S. A. Sabbagh, M. Sasao, G. Schilling, J. Schivell, G. L. Schmidt, S. D. Scott, R. Sissingh, C. H. Skinner, J. A. Snipes, J. Stevens, T. Stevenson, B. C. Stratton, E. Synakowski, W. Tang, G. Taylor, J. L. Terry, M. E. Thompson, M. Tuszewski, C. Vannoy, A. von Halle, S. von Goeler, D. Voorhees, R. T. Walters, R. Wieland, J. B. Wilgen, M. Williams, J. R. Wilson, K. L. Wong, G. A. Wurden, M. Yamada, K. M. Young, M. C. Zarnstorff, and S. J. Zweben. Fusion power production from tftr plasmas fueled with deuterium and tritium. *Phys. Rev. Lett.*, 72:3526–3529, May 1994.

[54] R. J. Hawryluk, S. Batha, W. Blanchard, M. Beer, M. G. Bell, R. E. Bell, H. Berk, S. Bernabei, M. Bitter, B. Breizman, N. L. Bretz, R. Budny, C. E. Bush, J. Callen, R. Camp, S. Cauffman, Z. Chang, C. Z. Cheng, D. S. Darrow, R. O. Dendy, W. Dorland, H. Duong, P. C. Efthimion, D. Ernst, N. J. Fisch, R. Fisher, R. J. Fonck, E. D. Fredrickson, G. Y. Fu, H. P. Furth, N. N. Gorelenkov, B. Grek, L. R. Grisham, G. W. Hammett, G. R. Hanson, H. W. Herrmann, M. C. Herrmann, K. W. Hill, J. Hogan, J. C. Hosea, W. A. Houlberg, M. Hughes, R. A. Hulse, D. L. Jassby, F. C. Jobes, D. W. Johnson, R. Kaita, S. Kaye, J. S. Kim, M. Kissick, A. V. Krasilnikov, H. Kugel, A. Kumar, B. Leblanc, F. M. Levinton, C. Ludescher, R. P. Majeski, J. Manickam, D. K. Mansfield, E. Mazzucato, J. McChesney, D. C. McCune, K. M. McGuire, D. M. Meade, S. S. Medley, R. Mika, D. R. Mikkelsen, S. V. Mirnov, D. Mueller, A. Nagy, G. A. Navratil, R. Nazikian, M. Okabayashi, H. K. Park, W. Park, S. F. Paul, G. Pearson, M. P. Petrov, C. K. Phillips, M. Phillips, A. T. Ramsey, M. H. Redi, G. Rewoldt, S. Reznik, A. L. Roquemore, J. Rogers, E. Ruskov, S. A. Sabbagh, M. Sasao, G. Schilling, J. Schivell, G. L. Schmidt, S. D. Scott, I. Semenov, C. H. Skinner, T. Stevenson, B. C. Stratton, J. D. Strachan, W. Stodiek, E. Synakowski, H. Takahashi, W. Tang, G. Taylor, M. E. Thompson, S. Von Goeler, A. Von Halle, R. T. Walters, R. White, R. M. Wieland, M. Williams, J. R. Wilson, K. L. Wong, G. A. Wurden, M. Yamada, V. Yavorski, K. M. Young, L. Zakharov, M. C.

Zarnstorff, and S. J. Zweben. Fusion plasma experiments on tftr: A 20 year retrospective. *Physics of Plasmas*, 5(5):1577–1589, 1998.

[55] Craig Beidler, Günter Grieger, Franz Herrnegger, Ewald Harmeyer, Johann Kisslinger, Wolf Lotz, Henning Maassberg, Peter Merkel, Jürgen Nührenberg, Fritz Rau, Jörg Sapper, Francesco Sardei, Ruben Scardovelli, Arnulf Schlüter, and Horst Wobig. Physics and engineering design for wendelstein vii-x. *Fusion Technology*, 17(1):148–168, 1990.

[56] A Iiyoshi, A Komori, A Ejiri, M Emoto, H Funaba, M Goto, K Ida, H Idei, S Inagaki, S Kado, O Kaneko, K Kawahata, T Kobuchi, S Kubo, R Kumazawa, S Masuzaki, T Minami, J Miyazawa, T Morisaki, S Morita, S Murakami, S Muto, T Mutoh, Y Nagayama, Y Nakamura, H Nakanishi, K Narihara, K Nishimura, N Noda, S Ohdachi, N Ohyabu, Y Oka, M Osakabe, T Ozaki, B.J Peterson, A Sagara, S Sakakibara, R Sakamoto, H Sasao, M Sasao, K Sato, M Sato, T Seki, T Shimozuma, M Shoji, H Suzuki, Y Takeiri, K Tanaka, K Toi, T Tokuzawa, K Tsumori, K Tsuzuki, K.Y Watanabe, T Watari, H Yamada, I Yamada, S Yamaguchi, M Yokoyama, R Akiyama, H Chikaraishi, K Haba, S Hamaguchi, M Iima, S Imagawa, N Inoue, K Iwamoto, S Kitagawa, J Kodaira, Y Kubota, R Maekawa, T Mito, T Nagasaka, A Nishimura, C Takahashi, K Takahata, Y Takita, H Tamura, T Tsuzuki, S Yamada, K Yamauchi, N Yanagi, H Yonezu, Y Hamada, K Matsuoka, K Murai, K Ohkubo, I Ohtake, M Okamoto, S Satoh, T Satow, S Sudo, S Tanahashi, K Yamazaki, M Fujiwara, and O Motojima. Overview of the large helical device project. *Nuclear Fusion*, 39(9Y):1245–1256, sep 1999.

[57] C. A. Haynam, P. J. Wegner, J. M. Auerbach, M. W. Bowers, S. N. Dixit, G. V. Erbert, G. M. Heestand, M. A. Henesian, M. R. Hermann, K. S. Jancaitis, K. R. Manes, C. D. Marshall, N. C. Mehta, J. Menapace, E. Moses, J. R. Murray, M. C. Nostrand, C. D. Orth, R. Patterson, R. A. Sacks, M. J. Shaw, M. Spaeth, S. B. Sutton, W. H. Williams, C. C. Widmayer, R. K. White, S. T. Yang, and B. M. Van Wonterghem. National ignition facility laser performance status. *Appl. Opt.*, 46(16):3276–3303, Jun 2007.

[58] R K Kirkwood, J D Moody, J Kline, E Dewald, S Glenzer, L Divol, P Michel, D Hinkel, R Berger, E Williams, J Milovich, L Yin, H Rose, B MacGowan, O Landen, M Rosen, and J Lindl. A review of laser–plasma interaction physics of indirect-drive fusion. *Plasma Physics and Controlled Fusion*, 55(10):103001, sep 2013.

[59] L J Atherton. Targets for the national ignition campaign. *Journal of Physics: Conference Series*, 112(3):032063, may 2008.

[60] John D. Lindl, Peter Amendt, Richard L. Berger, S. Gail Glendinning, Siegfried H. Glenzer, Steven W. Haan, Robert L. Kauffman, Otto L. Landen, and Laurence J. Suter. The physics basis for ignition using indirect-drive targets on the national ignition facility. *Physics of Plasmas*, 11(2):339–491, 2004.

[61] S. W. Haan, J. D. Lindl, D. A. Callahan, D. S. Clark, J. D. Salmonson, B. A. Hammel, L. J. Atherton, R. C. Cook, M. J. Edwards, S. Glenzer, A. V. Hamza, S. P. Hatchett, M. C. Herrmann, D. E. Hinkel, D. D. Ho, H. Huang, O. S. Jones, J. Kline, G. Kyrala, O. L. Landen, B. J. MacGowan, M. M. Marinak, D. D. Meyerhofer, J. L. Milovich, K. A. Moreno, E. I. Moses, D. H. Munro, A. Nikroo, R. E. Olson, K. Peterson, S. M. Pollaine, J. E. Ralph, H. F. Robey, B. K. Spears, P. T. Springer, L. J. Suter, C. A. Thomas, R. P. Town, R. Vesey, S. V. Weber, H. L. Wilkens, and D. C Wilson. Point design targets, specifications, and requirements for the 2010 ignition campaign on the national ignition facility. *Physics of Plasmas*, 18(5):051001, 2011.

[62] B. Remington, Lawerence Atherton, L. Benedetti, L. Berzak-Hopkins, David Bradley, Debra Callahan, D.T. Casey, P. Celliers, C. Cerjan, D. Clark, Eduard Dewald, T. Dittrich, S. Dixit, T. Döppner, Dana Edgell, M. Edwards, Reuben Epstein, J. Frenje, M. Gatu-Johnson, and S. Weber. Hydrodynamic instabilities and mix studies on nif: predictions, observations, and a path forward. *Journal of Physics: Conference Series*, 688:012090, 03 2016.

[63] John Lindl. Development of the indirect-drive approach to inertial confinement fusion and the target physics basis for ignition and gain. *Physics of Plasmas*, 2(11):3933–4024, 1995.

[64] Steven W. Haan, Stephen M. Pollaine, John D. Lindl, Laurance J. Suter, Richard L. Berger, Linda V. Powers, W. Edward Alley, Peter A. Amendt, John A. Futterman, W. Kirk Levedahl, Mordecai D. Rosen, Dana P. Rowley, Richard A. Sacks, Aleksei I. Shestakov, George L. Strobel, Max Tabak, Stephen V. Weber, George B. Zimmerman, William J. Krauser, Douglas C. Wilson, Stephen V. Coggeshall, David B. Harris, Nelson M. Hoffman, and Bernhard H. Wilde. Design and modeling of ignition targets for the national ignition facility. *Physics of Plasmas*, 2(6):2480–2487, 1995.

[65] J Lindl. *Inertial confinement fusion*. AIP-Press S. American Institute of Physics, New York, NY, May 1998.

[66] Stephen E. Bodner, Denis G. Colombant, John H. Gardner, Robert H. Lehmberg, Stephen P. Obenschain, Lee Phillips, Andrew J. Schmitt, John D. Sethian, Robert L. McCrory, Wolf Seka, Charles P. Verdon, James P. Knauer, Bedros B. Afeyan, and Howard T. Powell. Direct-drive laser fusion: Status and prospects. *Physics of Plasmas*, 5(5):1901–1918, 1998.

[67] Bedros Afeyan and Stefan Hüller. Optimal control of laser plasma instabilities using spike trains of uneven duration and delay (STUD pulses) for ICF and IFE. *EPJ Web of Conferences*, 59:05009, 2013.

[68] Stefan Hüller and Bedros Afeyan. Simulations of drastically reduced SBS with laser pulses composed of a spike train of uneven duration and delay (STUD pulses). *EPJ Web of Conferences*, 59:05010, 2013.

[69] R. Dragila. Second-harmonic generation at resonance absorption and modified plasma density profile. *Journal of Applied Physics*, 53(2):865–867, 1982.

[70] E. A. McLean, J. A. Stamper, B. H. Ripin, H. R. Grie, F J. M. McMahon, and S. E. Bodner. Harmonic generation in nd:laser-produced plasmas. *Applied Physics Letters*, 31(12):825–827, 1977.

[71] K. Eidmann and R. Sigel. Second-harmonic generation in an inhomogeneous laser-produced plasma. *Phys. Rev. Lett.*, 34:799–802, Mar 1975.

[72] T Ma, D Mariscal, R Anirudh, T Bremer, B Z Djordjevic, T Galvin, E Grace, S Herriot, S Jacobs, B Kailkhura, R Hollinger, J Kim, S Liu, J Ludwig, D Neely, J J Rocca, G G Scott, R A Simpson, B S Spears, T S Spinka, K Swanson, J J Thiagarajan, B Van Essen, S Wang, S C Wilks, G J Williams, J Zhang, M C Herrmann, and C Haefner. Accelerating the rate of discovery: toward high-repetition-rate HED science. *Plasma Physics and Controlled Fusion*, 63(10):104003, sep 2021.